The Effect of Opioids on Biomechanical Parameters of Bone

by Sydney Quinn Chizmeshya

A thesis submitted to the School of Graduate Studies in partial

fulfilment of the requirements for the degree of

Master of Science in Medicine.

Under the supervision of Dr. J. M. Andronowski

Faculty of Medicine, Division of Biomedical Sciences

Memorial University of Newfoundland

St. John's, Newfoundland, Canada

May, 2024

Table of Contents

Abstract

Bone is a dynamic and living tissue that continuously undergoes change throughout life. Current literature indicates that prolonged opioid exposure disrupts bone remodeling by inhibiting osteoblast activity and predisposing individuals to increased bone failure resistance. Our study builds upon proof-of-principle data from a pre-clinical rabbit-opioid model system to investigate 1) the biomechanical impact of opioid exposure on bone failure resistance, 2) the relationship between cross-sectional geometric values and fracture patterns, and 3) how microstructural parameters inform bone failure resistance. ***We hypothesize that bone specimens from opioid animals will demonstrate increased bone failure resistance, increased medullary area and cortical porosity, decreased cortical area and a diminished cellular network (e,g., lacunar parameters).***

Twenty-one male, skeletally mature New Zealand White rabbits were divided into three groups of seven animals each: morphine sulphate, fentanyl, and controls for eight weeks of experimental drug treatment. A multi-modal approach was used to collect data including high-resolution imaging (SRμCT) and biomechanical 3-point bend tests. Analyses revealed significantly greater cortical porosity in the morphine group compared to fentanyl and control animals. When examining the graphs visually, opioid groups demonstrated greater cortical and medullary areas and diminished markers of structural competence compared to controls. Analyses revealed that increased lacunar parameters are associated with reduced structural competence. Increased cortical area and medullary area are positively correlated with structural competence. Ultimately, evidence suggests that opioid exposure stimulated cellular dysregulation of the remodeling process and increased bone failure resistance in the opioid experimental groups.

Summary

Bone is a dynamic and living tissue that constantly adapts to our lifestyle and activity. Current research suggests that long-term opioid use can cause greater bone failure resistance by impacting bone cell functions that maintain bone strength and structure. Our study builds on a previous study to examine how opioid use, bone shape, and microstructure, inform bone failure resistance. We hypothesize that bone samples from opioid animals will require less force to induce fracture, experience greater bone failure resistance, have thinner bone cortices, and increased cortical porosity.

Twenty-one male, skeletally mature, New Zealand White rabbits were divided into three treatment groups of seven animals each: morphine sulphate, fentanyl, and controls for eight weeks of experimental treatment. High-resolution X-ray imaging experiments were performed to capture bone microstructure, and bending tests were performed to associate structure with function. We found that morphine animals displayed greater bone porosity compared to fentanyl and control groups. Ultimately, we found that opioid exposure was associated with dysregulation of bone cell maintenance and increased bone failure resistance in the opioid experimental groups.

Acknowledgments

First and foremost, this body of work would not be possible without the unfaltering support and expert guidance of my wonderful supervisor, Dr. Janna Andronowski. I thank her for her tremendous patience and dedication to her students and field. Under her tutelage, I have learned many new skills, discovered new passions, and I feel very lucky to be her student.

To the Andronowski Lab, I owe many thanks. They have been generous with their time, patient with my many questions, and supportive throughout this journey. Special thanks to Josh Taylor and Medhat Hassan for their instrumental support in the extremely computationally heavy image-processing aspects of this project. Many thanks to Shreya Hande, who provided much guidance and emotional support concerning my statistical queries, among other things. Thank you also to Zach Porter, David Benin, and Nafiza Haque for your positivity, comradery, and support. To future Andronowski Lab students, you are in exceptionally good hands.

I would like to extend my sincerest thanks to Dr. Dan Romanyk and Timothy Gadzella for their collaboration and expertise in this project, it would not have been possible without you. Thank you to Dr. Mike Wahl for your enthusiastic encouragement of adventure and reminding us to foster balance in our lives. Many thanks to my advisory committee, Dr. Ken Kao and Dr. Guangju Zhai, who generously provided knowledge and expertise. Thank you to the beamline scientists, Drs. Adam Webb, Ning Zhu, and Sergey Gasilov, at the Canadian Light Source Synchrotron facility for facilitating our imaging experiments and supporting us 24/7. I'd also like to mention the Canadian Institute of Health Research and the Faculty of Medicine (MUN), who financed my research during this program.

I feel so incredibly grateful to my best friends whom I met in this beautiful province, Maggie Deering, and Jenn Zagrodnik. You made hard days easy and bring sunshine wherever you go. Thank you for your unwavering support on this journey. Thank you to my incredibly supportive partner, Michael, who could probably recite the majority of my presentations from having listened to them so many times. Lastly, I am grateful to my parents, Gord and Karen Chizmeshya, for making sure I am never without, always bringing me home for Christmas, and always encouraging me in any direction I choose.

Credit Statement

1) Sydney Chizmeshya: *Methodology (CLS SRμCT experimentation, deep learning model design, biomechanical experiments, cross-sectional data acquisition); Data Acquisition; Writing (original draft); Writing (review and editing); Figure Preparation; Data Analysis/Interpretation; Date Visualization; Approving Final Version of Manuscript.*

2) Janna Andronowski: *Conceptualization; Project Design; Methodology; Data Acquisition/Analysis/Interpretation; Project Administration; Supervision; Critical Revision of Manuscript; Writing (review and editing); Approving Final Version of Manuscript.*

3) Dan Romanyk: *Project Design; Methodology (biomechanical experimentation); Data Acquisition; Supervision; Critical Revision of Manuscript.*

4) Timothy Gadzella*: Project Design; Methodology (biomechanical experimentation & adaptation of formulae for strength and modulus calculations); Data Acquisition; Data Analysis/Interpretation, Supervision.*

5) Medhat Hassan & Joshua Taylor: *Methodology (CLS SRμCT experimentation & deep-learning model design)*.

List of Tables

List of Figures

List of Abbreviations

ACTH:	adrenocorticotropin (ACTH)
ANOVA:	analysis of variance
ARF:	activation, resorption, formation
BMD:	bone mineral density
BMIT-BM:	biomedical and therapy bend-magnet beamline
BMP:	bone morphogenic proteins
BMU:	basic multicellular unit
CA:	cortical area
CIHR:	Canadian Institute of Health Research
CLS:	Canadian Light Source synchrotron facility
CNN:	convolutional neural network
CRH:	corticotropin-releasing hormone
CSA:	cross-sectional area
CT:	computed tomography
DHEA:	dehydroepiandrosterone
DHEAS:	dehydroepiandrosterone sulphates
FDA:	American food and drug administration
FSH:	follicle-stimulating hormone
GnRH:	gonadotropin-releasing hormone
GUI:	graphic user interface
IACUC:	Akron Institutional Animal Care and Use Committee
LH:	luteinizing hormone

LINAC:	linear accelerator
MA:	endosteal/medullary area
MA-Net:	multi-scale attention net
M-CSF:	macrophage colony-stimulating factor
MUN:	Memorial University of Newfoundland
NIJ:	National Institute of Justice
NZW:	New Zealand white rabbits
OPG:	osteoprotegerin
PBS:	phosphate buffered saline
RANK:	receptor activator of nuclear factor kappa beta
RANKL:	receptor activator of nuclear factor kappa beta ligand
SD:	standard deviation
SRμCT:	synchrotron radiation based micro-computed tomography
TA:	subperiosteal area
VOI:	volume of interest

1. Introduction & Literature Review

1.1 Bone Tissue

Bone is a dynamic and living tissue that continuously undergoes change throughout life. It can perform homeostatic functions, repair microdamage, and adapt to load-bearing stimuli. The skeletal system performs numerous functions for the human body, including to provide structure, protect vital organs, produce red blood cells, and act as a reservoir for calcium [1,2]. The skeleton is composed of various bone elements and tissue types, rendering this system flexible, strong, and resilient against mechanical strains such as bending, compression, tension, torsion, and shearing forces experienced in routine movement and locomotion [3]. On a molecular level, bone tissue is composed of protein collagen (e.g. collagen fibers, y-carboxylated proteins), calcium hydroxyapatite, and water [1,3].

At the gross level, bone tissue is composed of two types of tissue: Cortical, which is compact and dense, and cancellous bone (also referred to as trabecular/spongy bone) which demonstrates a porous structure with an organization of supporting rods and struts [2,3]. In total, the adult skeleton is composed of approximately 80% cortical and 20% cancellous bone [1]. Subchondral bone, a third bone tissue type, lies beneath cartilaginous joint surfaces and works to reinforce bone during locomotion at the location of the joint surfaces [3]. Cancellous bone is found at the articulating ends of long bones (epiphyses) and within vertebral bodies and houses red marrow [3]. Conversely, cortical bone composes the diaphysis (shafts) of long bones and encases a medullary cavity for the storage of yellow marrow [3]. During life, the periosteum (a fibrous, vascularized soft tissue membrane) covers the cortical bone's outer surface and works to provide nourishment and, in some cases, attachment for surrounding musculature [3]. Similarly, the inner

surface of bone is lined with a vascularized membrane called the endosteum [3]. Both the periosteum and endosteum work to support bone cells for the renewal and repair of bone tissue [3].

Embryologically, bone development can occur in one of two ways: intramembranous and endochondral ossification [2,3]. Intramembranous ossification is described as the ossification of bone tissue from within a sheath of mesenchymal cell membranes, such as the frontal and parietal bones of the cranial vault [1–3]. Endochondral ossification is described as the ossification of preceding hyaline cartilage [1–3].

Bone achieves its gross-anatomical shape and size through the modelling process [1–5]. Bone modelling describes the constant deposition of new bone on the periosteal surface and removal of bone tissue on the endosteal surface that occurs from infancy to adulthood. Bone modelling is activated in response to mechanical stimulus and facilitates the transition from the ~300 element infantile skeleton to the skeletally mature adult skeleton which comprises 206 elements [1–5]. During this developmental stage of the human skeleton, there exist numerous factors that can impact bone quality, fragility, and morphology (e.g., sex, age, nutrition, genetics, activity, and lifestyle factors [2,3,6–9]. Upon skeletal maturity, modelling will slow dramatically, and the maintenance and bone homeostasis will become regulated predominantly by the bone remodelling process [10].

1.2 Bone Microstructure and Remodelling

Beginning in utero and continuing throughout life, the bone remodelling process describes bone's performance of renewal and repair via secondary bone tissue creation (turnover) in cortical and trabecular bone tissue [1–5,11,12]. remodelling works to repair microdamage, maintain

strength, and regulate healthy ranges of serum calcium within the bone matrix by releasing minerals as required [1]. According to Walsh (2015), approximately 5-10% of the adult skeleton is remodelled each year [1]. However, remodelling rates can vary between individuals, within a skeleton, between sampling locations on a given skeletal element, and even vary within a cross-section of a singular element [4,13].

Microscopically, there exists canals within the bone matrix. “Primary canals" within bone are characterized by their appearance on both periosteal and endosteal surfaces [14]. Secondary osteonal systems (Haversian canals/systems) are especially associated with lamellae and are the structural location of bone remodelling [15–17]. It is within the boundaries of these secondary osteons that the remodelling process takes place and works to create and reinforce bone tissue [4,18]. First described by Frost (1986), the remodelling process is the activation of bone cells on the bone surface to perform the organized replacement of both secondary osteon in cortical bone tissues and hemi-osteons in trabecular bone tissue [1,2,4,19–21]. This process, as summarized by the activation-resorption-formation (ARF) sequence, is estimated to take 12 weeks’ time to complete [22,23]. Bone achieves remodelling by activating complex groups of cells known as basic multicellular units (BMUs) that include osteoclasts (bone resorbing cells) and osteoblasts (bone forming cells) [2,4].

The ARF sequence, while simplified to three phases, can be best explained in six detailed phases: activation, resorption, reversal, formation, mineralization, and return to quiescence [9,18]. In activation (1), osteoclasts and osteoblasts are activated, undergo maturation from their precursory form, and are called to a region in need of remodelling [9]. At this time, osteoclasts will commence the resorption phase (2) by binding themselves to the bone surface to secrete hydrogen ions and enzymes (i.e., cathepsin K, matrix metalloproteinases) which work to

disintegrate the bone matrix [1–3,9,21]. Osteoclasts will preferentially target locations of microcracks to efficiently remove compromised tissue [21]. The reversal phase (3) constitutes the cessation of osteoclastic resorption and osteoblasts are recruited to the resorption site [24]. Osteoblasts work to perform bone formation (4) by synthesizing a collagen-rich osteoid matrix in the form of concentric rings called lamellae [1,3]. This osteoid matrix undergoes mineralization (5), wherein the osteoid secretion becomes solid and remaining osteoblasts become trapped in the bone matrix [1–3,9,21]. During the final phase of quiescence (6), the trapped osteoblasts become bone lining cells, or osteocytes, that remain in the bone matrix and work to release calcium, act as mechanosensors, and signal for remodelling [1–3,9,21].

BMU activity and the ARF sequence are largely described and visualized in the literature as using an osteoclastic cutting-cone that creates tunnel-shaped resorption spaces [2,4,8,11,19,21] (**Figure 1**). Osteoblastic bone formation follows closely behind the cutting-cone laying down a new bone matrix in the form of concentric rings called lamellae surrounding a central Haversian canal for the passage of blood supply and innervation [3,7,9,10,12,14](**Figure 1**). The two groups of BMUs are considered both spatially and temporally "coupled" to equalize the amount of bone formation to resorption [1,25]. While the work of the bone-forming osteoblasts and bone-resorbing osteoclasts are inextricably linked, the rate of activity of these BMUs can cause adverse impacts on bone quality and quantity. For instance, apparent decreases in cortical porosity may be the result of an increased bone resorption, a depression in formation, or some combination thereof [12]. Alternatively, there could be an arrest during the reversal phase of the ARF sequence, thus "uncoupling" the process [26–28]. This process of remodelling produces osteons: the basic histological unit of bone [2,3]. Osteons can be further subdivided into two groups: primary and secondary osteons [2,3]. remodelling occurs at the location of secondary osteons [1,2,4,19–21].

Within secondary osteons, a reversal zone (demarcated by a 'cement line') separates the cutting cone of osteoclasts and group of osteoblasts [25].

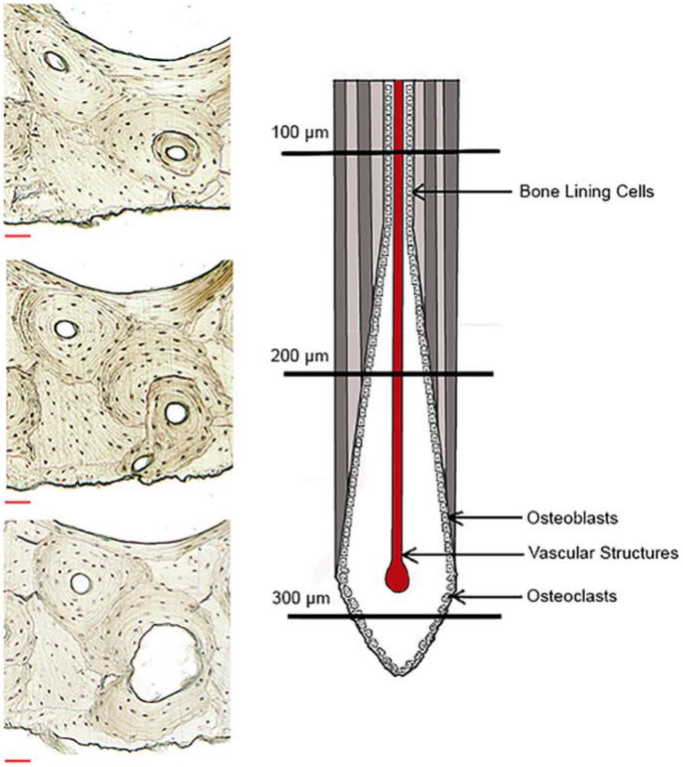

Figure 1: *Diagram illustrates variation in osteon morphometry and BMU activity depending on cross-sectional place alignment with associated histological sections. Serial sections: human, midshaft 6th rib demonstrating Haversian system remodelling from a complete secondary osteon after the closing cone (100µm depth) to a resorption bay at the cutting cone (300µm depth). Scale bar set to 100µm.* ***Figure credit:*** *Andronowski & Cole, 2020, WIREs Forensic Science.*

Osteoclasts evolve from hematopoietic stem cells into their pre-osteoclast/mononucleated cells, and eventually, osteoclast precursors that enter the bloodstream [1–3,21]. These osteoclast precursors emerge near the site that required remodelling and are introduced to macrophage colony-stimulating factor (M-CSF) and receptor activator of nuclear factor-kB ligand (RANKL) [1–3,21]. M-CSF will fuse with the osteoclast precursor cells while RANKL binds with receptor activator of nuclear factor-kB (RANK) on the surface of the pre-osteoclasts and inevitably create the maturation of multinucleated osteoclast cells [1–3,21].

If damage accumulates quicker than BMUs can perform this process of repair, larger microcracks will form and compound, forming a stress fracture [21]. To regulate bone resorption, a third important molecule is introduced: Osteoprotegerin (OPG) [21]. OPG is a secreted decoy

receptor that binds to the available RANK and inhibits the signalling required for further osteoclast differentiation [21]. This signalling axis composed of M-CSF, RANKL, and OPG are all produced by the osteoblast lineage cells and are highly susceptible to numerous influences including estrogen, testosterone, parathyroid hormone, vitamin D3, corticosteroids, and mechanical stimulus [1–3,21]. Conversely, osteoblasts differentiate from mesenchymal stem cells and this process is dependent on Runx2, bone morphogenic proteins (BMPs), and Wnt signaling [1].

Osteocytes, the most prevalent bone cell type, cover over 90% of the adult bone surface and outnumber BMUs in a ratio of approximately 20:1 [21]. Osteocytes are thought to be mechanosensors that reside within lacunae and work to detect mechanical stimuli via long dendritic processes that pass through the lacunar canalicular network [21,29]. Mechanical stimulation is thought to be a modulator of osteocyte apoptosis & induced resorption [21]. Too little mechanical stimulation causes osteocyte apoptosis via hypoxia mechanisms, while too much mechanical stimulation generates physical damage and induces apoptosis [6,30–35]. Osteocyte lacunae are described as being fluid-filled spaces wherein the fluid moves through the extracellular space during mechanical loading [21]. According to Robling et al (2001), the force of fluid movement is proportional to the mechanical loading rate, thus supporting conclusions that bone is more sensitive to dynamic loading than static loading [21,36]. Deformation of the bone matrix caused by mechanical loading is detected by these osteocytes, which then respond by sending paracrine signals to osteoblasts and osteoclasts via gap junction connections to begin the remodelling process [21].

1.3 Impact of Opioids on Bone

Previous work has demonstrated that BMU and bone remodelling function are subject to numerous physiological influences and lifestyle factors, including substance use [37]. Prolonged opioid use, for example, has demonstrated disruption to the bone remodelling processes and induces osteoporotic-like effects [38,39]. Clinically, opioids can be used as a treatment for moderate to severe pain; however, such treatments often require prolonged use, escalation of opioid doses and frequencies, and withdrawal symptoms after cessation (e.g., increased risk of infection, hyperactivity) [40,41]. Opioid use in a clinical setting has been shown to directly impact BMUs by inhibiting osteoblast activity, reducing bone formation, and predisposing individuals to bone fracturing and osteoporosis [42,43]. Furthermore, certain studies suggest that the use of opioids, such as morphine, for pain management may inevitably contribute to increased bone pain and a decrease in trabecular connectivity [40,42].

The current literature reflects three main hypotheses that describe the direct and indirect impacts of chronic opioid use on increased bone failure resistance [7]. First, opioids are reportedly correlated with an increased number of falls (indirect) due to their impact on the cranial nervous system as they can cause dizziness, somnolence, confusion, and sedation [7]. This finding is of particular interest because fracture-related falls are the sixth leading cause of death in elderly adults, a demographic in which opioid use for pain management is common [7,44,45]. Second, opioids are thought to reduce bone mineral density directly by reducing osteoblast activity in both human and animal analysis (direct), leading to a greater reduction of bone density via osteoclastic resorption [7,38,46–48]. Third, opioids have additional indirect effects on bone by dysregulating the complex mechanisms that regulate bone turnover (direct) [37,38,41–43]. By suppressing the hypothalamic-pituitary-gonadal axis, opioids inhibit the release of luteinizing hormone (LH),

follicle-stimulating hormone (FSH), and gonadotropin-releasing hormone (GnRH) in the pituitary gland [38,42,43]. The inhibition of these hormones catalyses a reduction in vital hormones such as estradiol and testosterone, resulting in hypogonadism/opioid-induced androgen deficiency, decreased bone mineral density, and osteoporosis [7,37,41,43]. The hormonal dysregulation of several other hormones has been observed in both men and women in clinical trials, for example: dehydroepiandrosterone (DHEA), dehydroepiandrosterone sulphates (DHEAS), adrenocorticotropin (ACTH) and corticotropin-releasing hormone (CRH), and cortisol [49–56].

1.4 The Opioid Crisis

The circumvention and clinical treatment of traumatic bone fractures are important considerations in modern health care. Opioid treatment regimens for pain management have been on the rise since the 1990s, and the recreational use of these analgesics has become an epidemic [57]. Canada has observed substantial increases in the amount of reported opioid toxicity deaths since 2016, and additionally report a continuation of this steady increase to the present day [58]. In 2020, many Canadian jurisdictions report an increase in fatal overdoses following the onset of the COVID-19 pandemic and the residual effects of this time continue to exacerbate the opioid crisis [57,58]. From January of 2016 to March of 2023, there have been over 38,000 reported opioid-toxicity deaths across Canada [58].

Opioid use and misuse continue to be a public health crisis nationwide. As such, it is increasingly important to understand the impact of these medications on bone quality and the remodelling process. Scholars have yet to discuss the impact of prolonged opioid use on bone's microstructural parameters, fracture patterns, and cross-sectional geometric values. This research speaks to specific demographics at greater risk and acts as a step towards modern understandings

of opioid-impact on bone failure resistance to better inform preventative measures and follow-up interventions for recovering opioid users.

1.5 Bone Biomechanics

The field of biomechanics deals with dynamic, biological materials from an engineering perspective to examine, analyze, and interpret behaviour within the context of a mechanical environment [59]. Bone is a dynamic, mechanosensitive tissue that is continuously adapting to its loading environment by altering its fibrous matrix and structure to accommodate load, and therefore, is biomechanically unique [21,59–61]. The structure of bone is representative of the bone's loading history throughout a lifetime [61]. Load bearing ability depends on the applied load and structural properties of the bone itself [61].

Bone biomechanical performance is predominantly based on three factors: bone mass, architecture and microarchitecture, and tissue material properties -- all of which differ between individuals and skeletal elements [51,53]. *Bone mass***,** also referred to as bone mineral density (BMD), is a description of mineral present in bone tissue at a given location or element and is the most studied determinant of bone structural behaviour [1–3,20,21,61–63]. It is frequently consulted in clinical settings, especially in elderly populations, post-menopausal women, and individuals at risk of suffering from osteoporosis. Because of this, BMD is considered a major predictor of bone failure resistance [2,3,22,60]. *Bone architecture* and microarchitecture describes the shape, structure, and organization of bone tissue [1–3,20,21,61–63]. Bone architecture is considered a key determinant of bone strength [1–3,20,21,61–63]. *Bone tissue material properties* are described as the properties of bone tissue independent of mass and structure [2,3,28,61,64]. These can be studied via biomechanical experimentation (mechanical loading experiments) that

produces numerous parameters that assist in characterizing bone's performance in a mechanical environment (i.e., stiffness, yield, peak load, strain, etc). While mass, architecture, and material properties of the skeleton determine bone strength and capacity for fracture resistance, many factors can compromise bone biomechanical performance such as ageing, trauma, nutrition, disease, substance use, activity, among others [61].

As a composite material, bone sustains numerous external forces throughout locomotion/mechanical loading and regularly resists bending, compressive, tensile, torsion, and shearing forces throughout routine movement [2,3,61]. The overuse of bone can lead to microcracks that stimulate bone remodelling for reparation [21]. Conversely, disuse or lack of loading can cause the atrophy of bone tissue, an acceleration of the bone turnover process, increased resorption, and a rapid loss of bone mass [2,21,36,59,61]. It is understood that periosteal bone formation steadily increases proportionally with increased loading, thus indicating that the mechanisms of bone remodelling and bone adaptation to loading differ [21]. The effects of elevated mechanical demands on bone are well documented. Smith and Walker (1964) demonstrated that long bones, such as femora, will continuously undergo diaphyseal expansion throughout adulthood as a result of mechanical loading [59,65]. This process of bone adaptation creates tissue bolstering in the direction of functional demand (anisotropy) [59]. Robling and Turner (2009) found that loading rat forelimbs led to a 64% increase in bone strength, however, only a 7% increase in bone mineral density [21]. This finding illustrates that loading improves bone biomechanical performance by improving mass and by becoming more structurally efficient in the adaptation of the loading process. Additionally, the literature reflects that mechanical loading can also impact bone microstructure and vice versa. For example, mechanical loading has been shown to create smaller and more circular osteons [66,67]. Smaller and more circular osteons

can be more densely packed in a given area of bone and are more mechanically advantageous as their circularity and reinforced border (cement lines) are better at deflecting microcracks [66–69].

Characterizing bone material properties may allow for the prediction of fracture resistance, bone failure resistance, and structural competence of bone [61], and as such, *cross-sectional geometry* can assist in this. Cross-sectional geometric properties measure the amount and the distribution of skeletal tissue [59]. This type of bone material characterization can be useful in predicting bone failure resistance and patterns in a skeletal element [59]. For example, cross-sectional area (CSA), subperiosteal area (TA), endosteal/medullary area (MA), and cortical area (CA) work to describe the bone mass represented by a geometric measure, whereas moments of inertia work to describe bone architecture/cross-sectional organization [59,61]. Moments of inertia are a geometric measure of a bone's distribution of material about a central location and informs the sample's resistance to loading and deformation [59,61]. To expand on the latter, consider two bone samples with the same amount of cortical bone mass. One of these samples has a larger medullary area, and the other, a smaller medullary area. The sample with the larger medullary area, and therefore a larger material distribution further away from the neutral axis, will be much stronger than the sample with a smaller medullary area [61]. Cross-sectional geometric analysis tells us that the morphology of a given diaphysis will primarily be influenced by bending and torsional forces due to this distribution of bone mass over a larger area [59].

The process of biomechanical experimentation can provide many parameters to help characterize bone's biomechanical performance. For example, *stiffness* describes a sample's ability to resist deformation and is determined by calculating the slope of the linear region in a force-displacement curve [61,70]. *Yield point* is the break from linearity seen in the force-

displacement curve and describes the force that initiates permanent deformity [61]. *Peak load* describes the maximum amount of force the sample can load [61]. *Failure point* is the force and/or displacement at which bone fractures completely and/or can no longer withstand applied load [61]. The fracture site in a given sample is often the site of minimum displacement [71]. *Stress* describes the magnitude of resistance against loading, *strain* describes the amount of deformation, and *strength*, also called the *ultimate point*, is the load required to fail the whole bone [61,72]. Strength of a sample is based on the chemical bonds of the mineral fibres present that connect the neighbouring cross-sectional areas [60]. Cortical geometry and porosity (intracortical canals, haversian systems, etc) are major determinants of bone stiffness and strength [73].

Biomechanical experimentation most often uses tibial, femoral and/or vertebral elements for experimental testing [74]. Of these samples, bend-testing is the most popular test for long bones, and compression is most often used for vertebral samples. When planning a biomechanical experiment, it is always ideal to use fresh bone samples that have not been exposed to preservation, heat, or dehydration [59,71,74–77]. Often, fresh samples are not available, and researchers will be obligated to use some to preserve bone samples. In this case, bones should be stored in a way that minimizes the alteration or degradation of bone's biomechanical properties. The conservative freezing and thawing of bone samples does not significantly impact the mechanical properties of bone [76,78]. Chemical fixation using aldehydes is not recommended as it has been shown to directly impact bone mechanical properties by interfering with the collagen in bone [74,77]. Nazarian et al., (2009) compared the biomechanical effects of fresh, frozen, and formaldehyde fixed femora and vertebral samples, finding that stiffness, elasticity, displacement, load, strain, and strength did not differ

significantly between groups [74]. Formaldehyde fixation, however, did impact bone's viscoelastic properties as well as both frozen and fixed groups required rehydration prior to biomechanical testing [74]. Dehydration of bone samples is possible during the freezing process but can be rectified by incorporating a rehydration protocol prior to mechanical loading. Broz et al. (1993) demonstrated that the original flexural properties of whole mouse femora were preserved by air dehydration and were recovered using a saline rehydration [78]. Additionally, they found that rehydration times demonstrated no difference past three hours [78].

1.6 Rabbits (Oryctolagus cuniculus) as a Model Organism

Human cortical bone, as with other large vertebrates, are dominated by secondary bone that is generated via the remodelling process. Conversely, smaller species of animals, including murine species, demonstrated little to no secondary osteonal remodelling/cortical bone turnover and therefore retained primary osteons throughout life [79–81]. The American Food and Drug Administration (FDA) thus recommends the use of larger animals who experience this cortical turnover for the purposes of osteoporosis research [82].

A rabbit model is the most appropriate model organism to use for human bone research because they are the smallest laboratory animal to demonstrate spontaneous cortical bone remodelling and display secondary osteons comparable to humans [19,21,83–86]. Rabbits experience a shorter remodelling period and become skeletally mature in as little as 6-9 months of age [87,88]. Previous studies have employed a rabbit model of a similar cohort size to that of this body of research to examine central canal size and vascular networks of cortical bone [84,85]. Based on this, a rabbit cohort of this size (N = 21) prove to be an extremely appropriate, and FDA-recommended model for bone biology and orthopaedic research [19,42,71,89–95].

1.7 Synchrotron Micro-CT Imaging

Synchrotron radiation-based micro-computed tomography (SRμCT) is a form of specialized, high resolution imaging experiments. Synchrotrons are mass particle accelerators that speed electrons at the speed of light to produce x-rays. Electrons are shot from an electron gun into an ultra-high vacuum chamber where they move from the cathode toward the linear accelerator (LINAC)[96]. The electrons travel from the LINAC and into a booster ring to raise their energy[96]. Once electrons reach 2900 MeV, they enter the storage ring[96]. The storage ring is a large ring composed of 12 straight chambers where electrons are accelerated around by radio frequency waves and electromagnets [96]. When the electrons round the corner of the connected straight chambers, they refract and produce *Bremsstrahlung* (*Breaking Radiation*) that emits a brilliant source of highly focused light (infrared and x-ray) [96]. The generated beams of light travel down a beamline where the light spectra are filtered by a monochromator [97]. The beamlines and endstations host light of specific wavelengths for different imaging experiments [96,97]. Various imaging techniques can be performed on various beamlines at a synchrotron facility. For example, the Biomedical Imaging and therapy beamline at the Canadian Light Source (CLS) Synchrotron facility (Saskatoon, SK) provides a resolution of 1-2μm and have allowed for the remarkable advancement of bone tissue visualization and analysis that was previously not possible in two-dimensional imaging or histological techniques [96–102].

1.8 Objectives and hypotheses

The current research project builds upon proof-of-principle data from a former Andronowski Lab National Institute of Justice-funded pre-clinical opioid animal model system [89]. Here, we investigate the 1) biomechanical impact of opioid exposure on bone failure

resistance, 2) create a novel Deep Learning model for the purposes of SRμCT feature segmentation, 3) the relationship between cross-sectional geometric values and fracture patterns, and 4) how microstructural parameters, such as cortical porosity and osteocyte lacunar density, inform bone failure resistance and fracture patterns as observed via synchrotron radiation-based micro-Computed Tomography (SRμCT). ***We hypothesize that a decrease in cortical area and lacunar density, an increase in cortical porosity, and enlarged medullary cross-sectional area will be observed in opioid animals compared to controls***. Further, by employing 3-point bend tests of long bones, ***we hypothesize that bone failure resistance will be increased in opioid animals, and that less force will result in bone failure and fracture in experimental animals.*** Results from the mechanical testing will be correlated with bone architectural properties (via synchrotron micro-CT) to associate structure with function and further elucidate expected indirect effects of opioid use on bone biomechanical performance.

2. Materials & Methodology

Our study employed a multi-modal approach to evaluate bone quality and bone failure resistance following opioid exposure in an opioid animal model system.

2.1 Rabbit-Opioid Experimental Model and Study Sample

The study sample included rabbit bone specimens from a former National Institute of Justice-funded preliminary longitudinal study from the Andronowski Lab (2018-DU-BX-0188) which developed a rabbit-opioid experimental model [89]. The experiments were performed at The University of Akron, Ohio in 2019, and were approved by The University of Akron Institutional Animal Care and Use Committee (IACUC) **(Appendix A).**

The animals consisted of healthy, skeletally mature, male New Zealand White (NZW) rabbits *(Oryctolagus cuniculus; n = 21)* acquired from Covance Research Products Inc. (Denver, PA, USA) [89]. Comparable to humans, rabbits demonstrate spontaneous cortical bone remodelling [84–86,89]. Smaller laboratory animals, such as murine models, for example, retain primary canals and do not significantly demonstrate spontaneous cortical bone remodelling, nor is there growth plate closure in rodent models indicating complete cortical fusion [84–86,89]. Additionally, rabbits are an effective model organism as they are skeletally mature in approximately 8 months [84]. Lastly, rabbits are an FDA recommended model organism for bone biology experimental research due to their comparable bone turnover processes [19,42,71,89–95]. The experimental cohort size used in this study reflects cohort sizes that are consistent with similar NZW rabbit studies on osteoporosis and bone remodelling [85,86,98,103,104].

Rabbits were individually housed in Allentown rabbit batteries with a 12:12/h light: dark cycle [89]. Rabbits received 150g chow/day (Harlan Teklad Global High Fiber Rabbit Diet) and water *ad libitum*, as well as enrichment foods (e.g., spinach, dried fruit, papaya tablets) provided daily and enrichment devices (e.g., rattles, jingles balls, flexi-keys) provided in rabbit batteries and exercise pens which they were placed in for forty-five minutes, three times a week [89]. The rabbits acclimatized for a two-week period prior to experimental treatments [89].

The animals were randomly divided into three groups of seven each: morphine, fentanyl, and controls [89]. Drug administration operated as follows: 3mg/kg/day of morphine sulphate was delivered via subcutaneous bolus injection; fentanyl was administered via transdermal patch on the interscapular region (25µg/h slow release) [89]. Similar to drug administration methods, the control group was further subdivided into a saline vehicle subcutaneous injection (3 mg/kg/day: *n=3*) and sham patch group (*n=4*) [89].

Following the acclimation period, treatments were applied to control and experimental groups for eight weeks [89]. Throughout the experimental period, daily and weekly observations were recorded (e.g., weight, fecal output, food consumption, behaviour, etc.) and subcutaneous injections with a bone-labelling fluorochrome (Calcein) were administered every two weeks at a level of 10 mg/kg [103]. Following euthanasia, rabbit hindlimbs, ribs, and vertebrae were collected and processed to remove soft tissues [103]. Analyses from this former Andronowski Lab initiative included micro-CT imaging, dynamic histomorphometry, and biomechanical testing [103]. Following euthanasia, left hindlimb bones (femora, tibio-fibulae) were macerated and prepared for the imaging using conventional desktop micro-computed tomography (µCT), dynamic histomorphometry, and SRµCT [89,102,103]. As such, ***the contralateral limbs (right side) were used for this project.*** Rabbit #5 (Control) was removed from the study due to

fractures in the right tibiofibulae that occurred during excision, thus reducing the study's population size from *n*=21 to *n*=20. Subsequent left tibial bone cores were collected and imaged for the sole purpose of this work as well as the remaining right tibiae to address novel biomechanical queries [102]. The bone-coring protocol was employed as per Andronowski et al., 2020 [102].

2.2 SRμCT Sample Preparation

Left tibial bone specimens were prepared for SRμCT imaging using a coring technique adapted for bone developed by Andronowski et al., 2020. Left rabbit hindlimb bones were cored using a mill-drill press and diamond coring bit to create consistent core diameters (1-5mm) cylinders [89,102]. All cores originated from the anterior mid-cortical region of the proximal left tibiae. Cores were stored individually in microcentrifuge tubes at ambient temperature until imaging experiments.

2.3 SRμCT Imaging

High-resolution SRμCT imaging experiments were performed on the Biomedical and Therapy bend-magnet Beamline (BMIT-BM) at the Canadian Light Source (CLS) national synchrotron facility in Saskatoon, SK. Specimens were mounted to sample holders and focused within a representative field of view via a goniometer and light microscopy set-up **(Figure 2, a.).** Goniometers were mounted into the beam path and confirmed to be in the field of view using the live view function of the graphic user interface (GUI) (**Figure 2, b.).** Schematic representation of BMIT-ID and sample setup visualized in **Figure 3.**

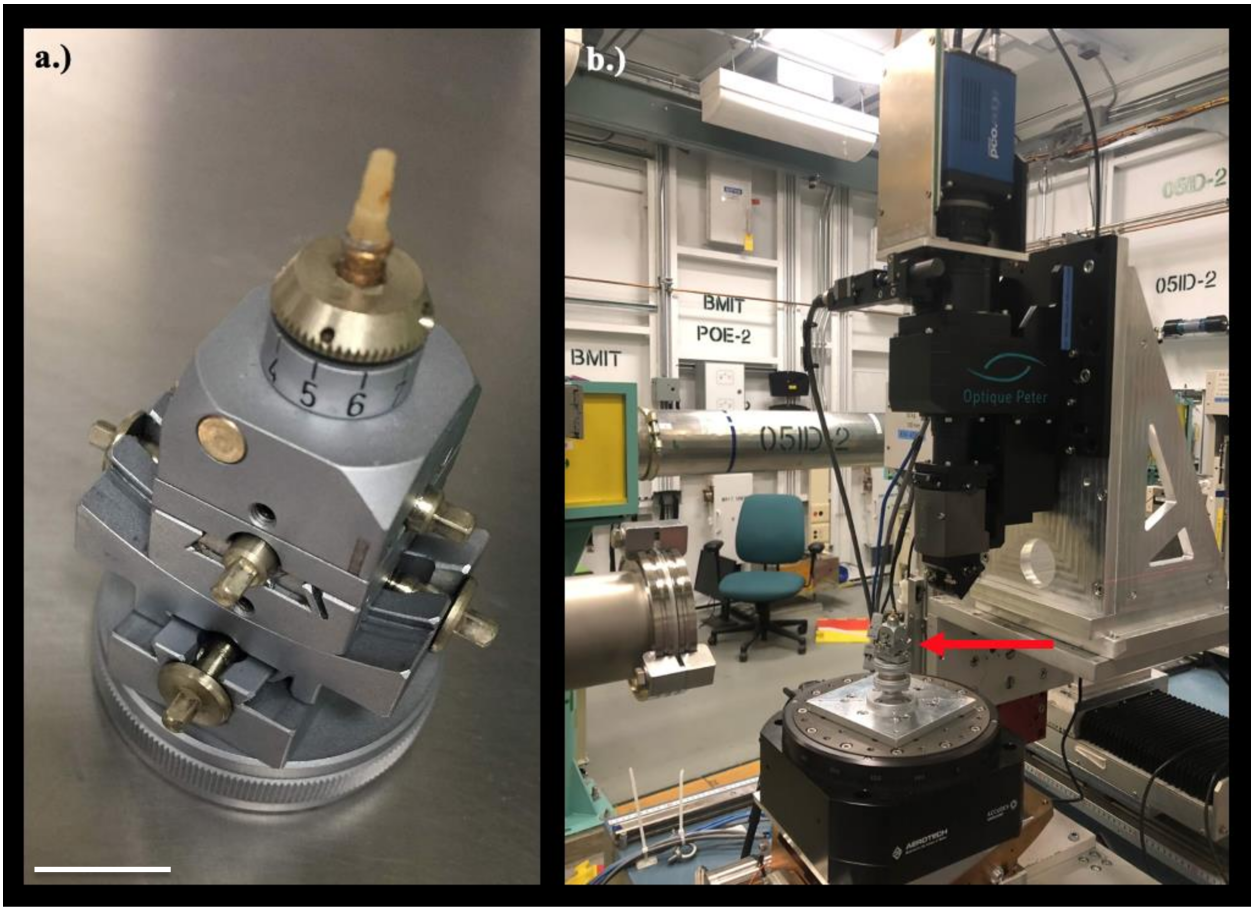

Figure 2: *Photos from SRμCT imaging experimental setup. a.) demonstrates bone sample core mounted onto goniometer. Scale bar set to 1cm. b.) demonstrates goniometer (demarcated by red arrow) mounted into beam path and in field of view of the live function graphic user interface.*

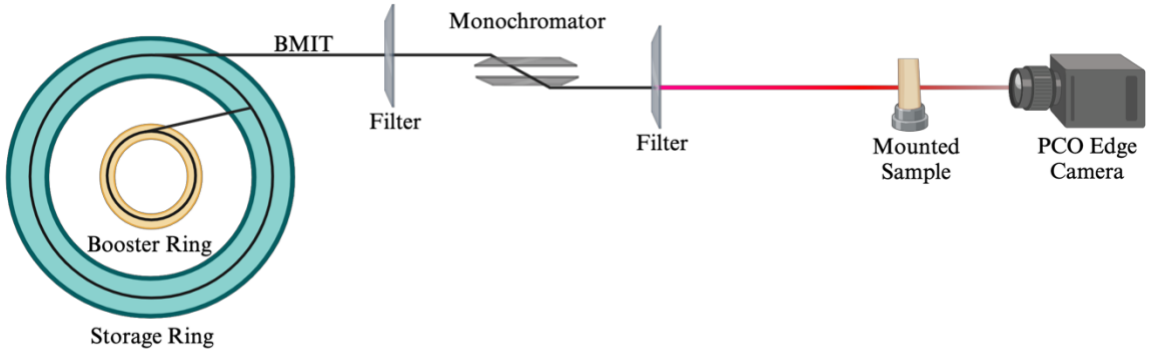

Figure 3. *Schematic representation of SRμCT experimental set up on the BMIT-ID beamline at the CLS. The sample is mounted to a rotary stage in which the beam crosses to record inner structures of the sample by the PCO edge camera. Figure created with Biorender.*

Due to the highly competitive nature and peer-reviewed beamtime for SRμCT imaging experiments, rabbit tibiae scans were divided into two separate experimental runs: September 27-29th of 2021 and September 13-16th of 2022. Funding and beamtime awards were secured by Dr. Janna M. Andronowski. The experimental parameters employed are available in **Table 1.** For further BMIT graphic user interface (GUI) parameters see **Appendices B and C**. Despite imaging being conducted over two separate imaging runs, the experiments remained comparable. Due to the variable current of the storage ring, X-ray exposure was adjusted throughout both experimental beamtimes to maintain 20% saturation on the detector.

Table 1: *Experimental parameters for September 2021 and September 2022 beamtimes.*

Experimental Details (Sept. 2021 & 2022)	
Beam type	White beam microscope
Objective	5x
Photon energy	20 keV
Pixel size (resolution)	1.5μm
Sample-detector distance	5cm
Filter types	0.8mm aluminum & 0.08mm molybdenum
Images captured per sample	3000
Frames per second (fps) rate	33
Step angle	0.06
Exposure (msec)	150
Trigger	External
Camera Type	PCO Edge
Storage ring current	Top-up mode

2.4 SRμCT Image Processing:

Each dataset was composed of raw SRμCT projections consisting of ~2300 transverse cross-sectional slices at a resolution of 1.5μm. Datasets were reconstructed into image stacks (3D volume) of 32-bit grayscale TIFF slides via ufo-kit software. Raw data reconstruction parameters are available in **Appendix D.**

To isolate and extract features of interest (e.g., vascular pores and osteocyte lacunae) from high-density bone, a custom image processing workflow was designed using ORS Dragonfly (Object Research Systems Inc., Montreal, Canada) interface and software packages DataViewer and CTAnalyser (v.1.18.4.0, Brucker, Kontich, Belgium) [104].

A uniform volume of interest (VOI) was isolated from the original dataset for each sample and manually segmented using Dragonfly's ROI thresholding function and manual brush tools to highlight pores and osteocyte lacunae. Multi-ROIs were created using ~2-5 manually segmented layers. A pre-trained deep learning model, multi-scale attention net (MA-Net), was employed to automate the segmentation process. This particular model introduced a self-attention mechanism to describe spatial and channel-wise relationships between pixels of an image [93] and is suitable for these data given it was trained on CT images of liver cells and tumors [93]. Multi-ROIs were used to further train MA-Net to our project's specifications (discerning vascular pores and osteocyte lacunae). The trained model was then tested on new samples from the dataset and compared to the traditionally segmented sample using ORS Dice Loss which provides a percentage of similarity that can be used to discern what model is most effective in its accurate labelling of features.

Multi-ROIs for pores and osteocyte lacunae used in training were created separately as it proved more accurate compared to training a single model to perform both pore and osteocyte

lacunar segmentation. After training and selection of the most suitable deep-learning model for the data, the MA-Net model was used to segment all 20 data sets and produce binary images of pores and lacunae, respectively (**Figure 4**). Microstructural parameters were exported via 3D custom image analysis in CTAnalyser using binary pore and lacunae image stacks. Parameters of interest included mean and standard deviation of pore thickness, mean and standard deviation of pore separation, average pore volume, pore segments mean radius, pore size (diameter), cortical percent porosity, canal surface density, pore connectivity density, and pore density.

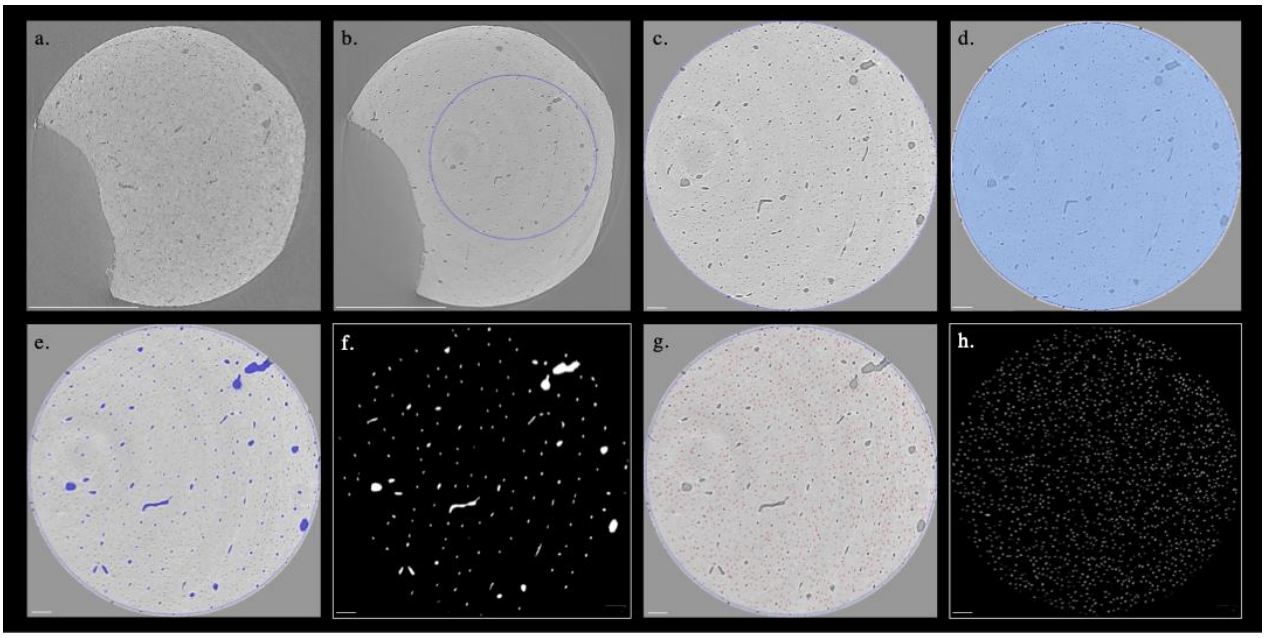

Figure 4. *Visualization of custom workflow in Dragonfly interface to permit feature segmentation and data extraction.* **a.)** *2D view of one image slice of complete sample reconstruction from a stack of 2161 image slices. Scale bar set to 1 mm.* **b.)** *A uniform region of interest (ROI) is selected from an image stack using the cylinder feature. Scale bar set to 1 mm.* **c.)** *Sample region of interest is isolated in a 3D stack. Scale bar set to 100µm.* **d.)** *A mask is applied to the ROI stack to apply the pre-trained deep learning model to apply pore and resorptive space segmentation (e.) and osteocyte lacunae segmentation (g.). Scale bar set to 100µm.* **e.)** *ROI with complete pore and resorptive space segmentation reflected in blue. Scale bar set to 100µm.* **f.)** *Binarized version of ROI with complete pore and resorptive space segmentation used for data extraction. Scale bar set to 100µm.* **g.)** *ROI with complete osteocyte lacunae segmentation reflected in red. Scale bar set to 100µm.* **h.)** *Binarized version of ROI with complete osteocyte lacunae segmentation used for data extraction. Scale bar set to 100µm.*

2.5 Biomechanical Sample Preparation

Following euthanasia, right tibio-fibulae were immediately frozen once procured from all rabbits. All samples were housed in a -20°C freezer and brought to room temperature prior to maceration. Right rabbit tibiae/fibulae were collected and macerated, fixed in 70% ethanol for 24h and subsequently wrapped in PBS or 0.9% saline collusion-soaked gauze and stored in air-tight containers in a -20□ freezer.

2.6 Biomechanical Testing

Biomechanical testing was performed in Dr. Dan Romanyk's Lab, School of Dentistry, University of Alberta in March 2023. Experiments were performed using an Instron E3000 Frame equipped with a 5kN load cell and 3-point bending apparatus and compression test plate on the right rabbit tibiae. All bend-test parameters were set using the associated Wavematrix software program and tests were recorded with a Basler ACA 1920 camera and Basler Pylon software to capture video footage of tests (**Figure 5**).

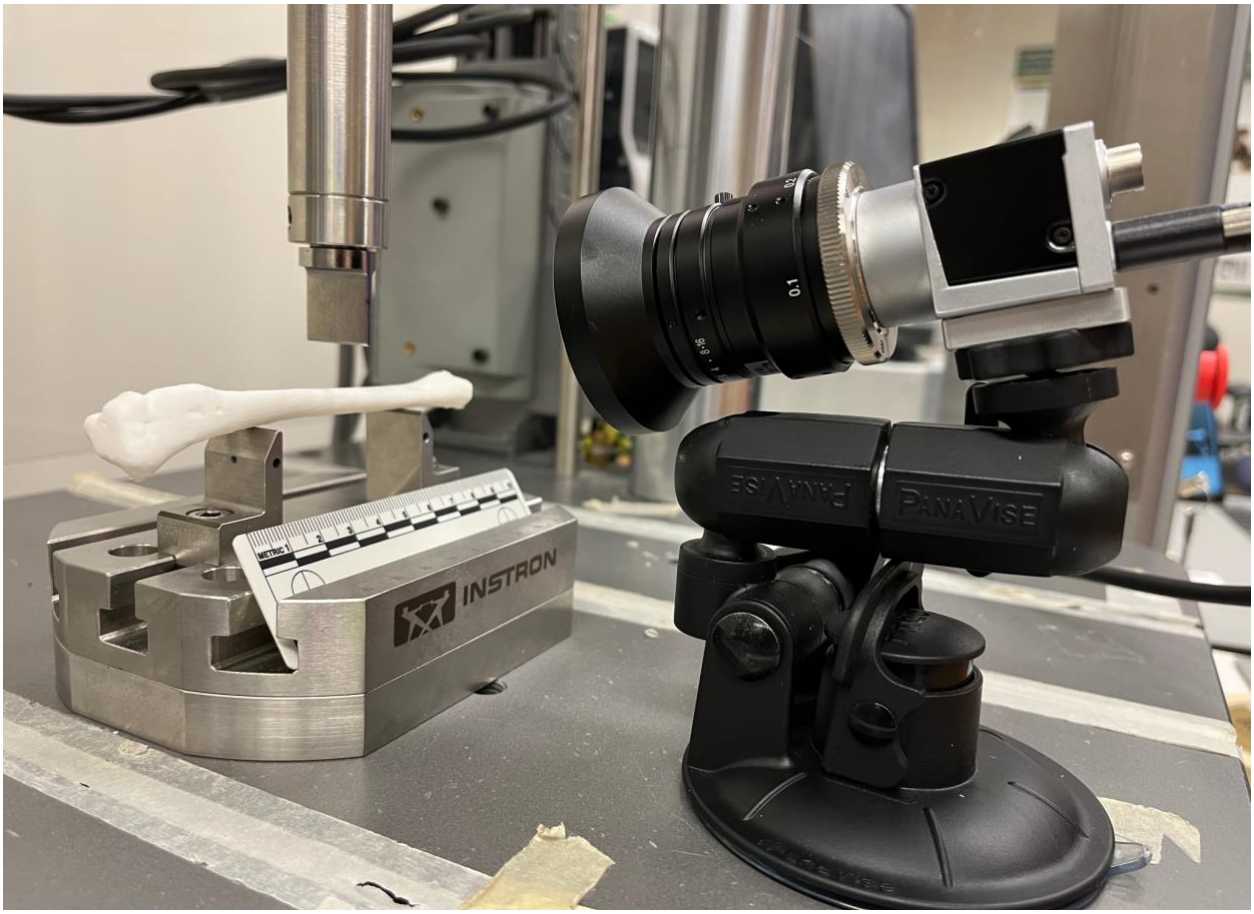

Figure 5. *Basler camera set up in front of 3-point bend testing anvils with 3D printed rabbit tibia set up for parameter testing, The University of Alberta, Dr. Romanyk Lab.*

Proximal rabbit fibulae were cut with a Dremel tool prior to testing to isolate the tibiae for biomechanical testing; this modification with isolate the bone experiencing loading during testing as well as stabilize the bone sample on the Instron anvils. Samples were rehydrated in diluted saline solution for 30 minutes prior to testing. After rehydration, each sample was photographed, the sample span (diaphyseal length) and midpoint were documented, and anvils were adjusted respectively for each sample. Posterior aspects of right rabbit tibiae were placed on the lateral anvils. A preload rate of 1 mm/min up to a 5N force was established to allow for good contact of central anvil at tibia midpoint (anterior aspect) followed by a five-second hold before the test began. The test loading rate was set to 1 mm/min following the completion of

preload and hold. Complete biomechanical test parameters can be seen in **Appendix E**. Samples were tested until either complete fracture or, if fracture could not be achieved, until the force plateaued post-failure (i.e., the weight-bearing plateau following the fracture and decay period of bending). Each bend test was recorded, and all sample fragments were collected, wrapped in saline gauze, and stored in a -20□ freezer.

2.7 Cross-sectional data acquisition:

To determine bone biomechanical properties, cross-sectional geometric properties are necessary to examine the raw 3-point bend test data. Using cross-sectional geometric data, we obtained variables such as strength, flexural modulus, and young's modulus that help describe the biomechanical performance of opioid-exposed bone during quasi-static testing.

Cross-sectional geometric values were obtained post-hoc from the fractured right tibial fragments. Proximal tibial fragments were cut using a Buehler Isomet 1000 precision saw just superior to the fracture point to produce a perpendicular transverse surface reflecting the sample's unique cross-section. Subsequently, the transverse cross-sectional surfaces of the samples were photographed with a scale using a dissection microscope and camera in the Gendron/Paradis Lab, MUN (**Figure 6, a**.). Images of each sample were manually segmented to reflect the cross-sectional surface only using Dragonfly interface, binarized, exported, and uploaded into ImageJ image processing program [105] (**Figure 6, b**.). The ImageJ plugin BoneJ was used to compute collections of bone specific variables such as cross-sectional area/cortical area (CSA), moments of inertia, and other cross-sectional geometric properties [106] (**Figure 6, c.**). The moment of inertia examined in this study was that of secondary moment of inertia about

the mediolateral axis (i.e., in the anterior-posterior direction), often denoted as IML[109]. The formula for this calculation as performed by BoneJ is as follows:

$$IML = I_{CM} + A \times d^{2}$$

In this equation, I_{CM} reflects moment of inertia about the center mass, A reflects the area of the object, and d reflects the perpendicular distance between the mediolateral axis and the center of mass[109].

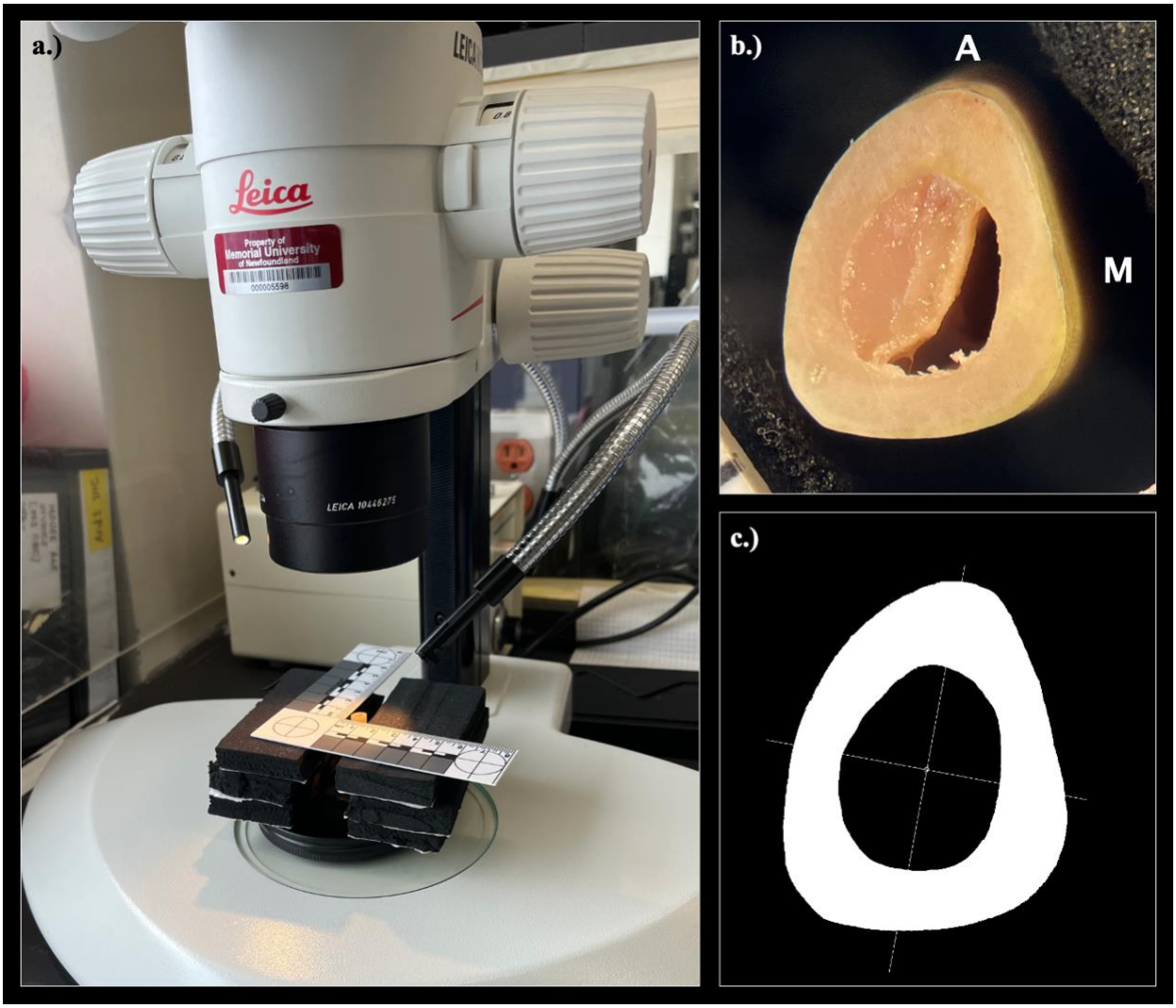

Figure 6: *Cross-sectional data acquisition after samples were cut superior to fracture site to create a flat surface: a.) transverse cross-sectional surfaces of proximal tibia were photographed with scale using a dissection microscope and camera in the Gendron/Paradis Lab,*

MUN. b.) photos of cross-sections were labeled with "A" for anterior and "M" for medial and a scale was set using ImageJ. c.) Cross-sectional surfaces were manually segmented in Dragonfly interface, binarized, and uploaded to ImageJ for cross-sectional data acquisition.

2.8 Biomechanical Data Acquisition and Calculations

Data from 3-point bend testing produced force-displacement curves that illustrate the biomechanical performance of the sample under loading conditions. The loading region of the force-displacement curve provide information regarding the sample's behaviour while resisting loading until the point of before permanent deformation (fracture) (**Figure 7**). Data of interest from the force-displacement curves (i.e., peak-load (N), displacement (mm), and test time (s)) was examined for differences between groups and relationships with SRμCT and cross-sectional geometric data.

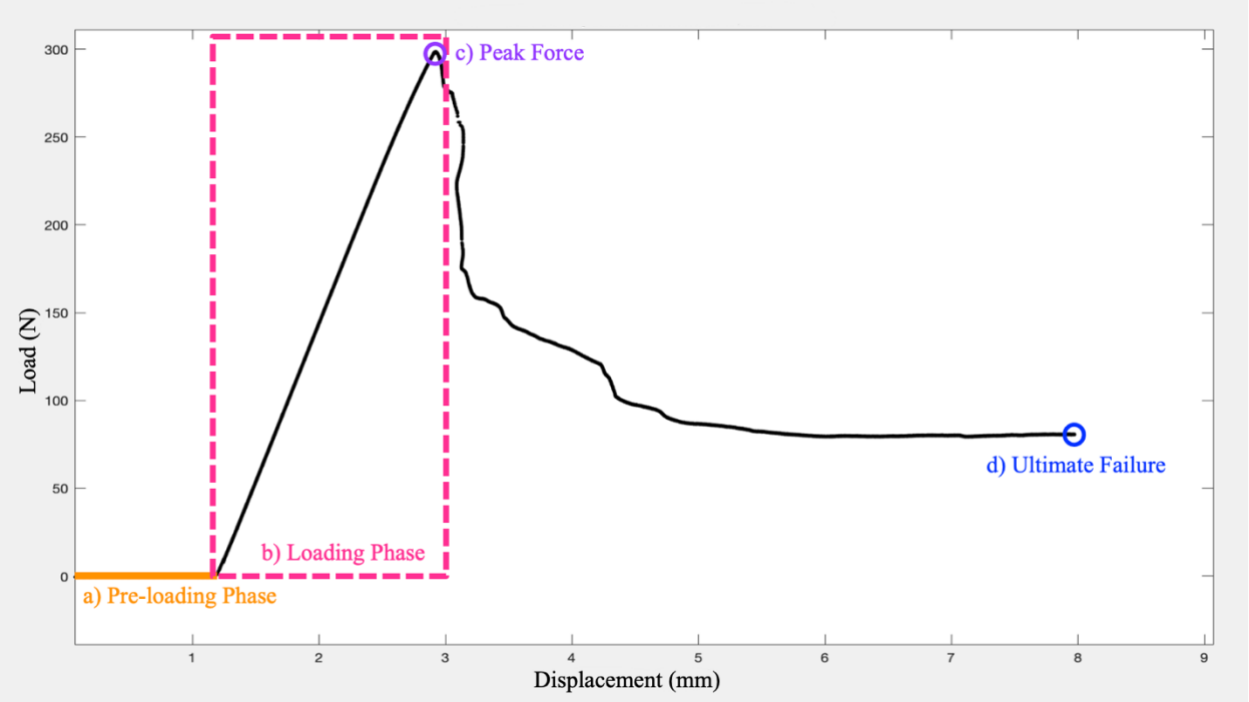

Figure 7. *Example force-displacement curve. a)* ***preloading phase*** *refers to phase 1 of bending protocol wherein the central anvil contacts the sample's midpoint, applies a predetermined load*

of 5N and holds for 10 seconds to ensure no movement of the sample on the testing apparatus. b) demonstrates a sharp linear region described as sample ***loading****, wherein the sample actively resists deformation. c)* ***peak force*** *describes the maximum amount of force applied to the sample during bending. d)* ***ultimate failure*** *is described as the point at which sample fibres can no longer withstand any force.*

Strength is a complex descriptor of bone biomechanical performance as it describes a sample's ability to resist fracture/failure during loading, whereas ***Flexural modulus*** is a material property that describes a sample's stiffness and resistance to bending [59,61].

The material and structural property of bone determine its behaviour under load [107–109]. Thus, both the biomechanical and cross-sectional geometric data can be used to calculate strength, flexural and young's moduli.

Table 2. *Demonstrating formulae used to calculate Strength, Flexural Modulus, and Young's Modulus, complex descriptors of bone biomechanical performance under bending.*

Variable	Unit	Definition	Equation	Variable Description
Strength	MPa	ability to resist failure	MY/I	M = (span in mm÷ 2)*peak-force (N)
				Y = posterior cortical wall thickness (mm)
				I = moment of inertia (mm^4)
Flexural Modulus	MPa* mm^4	ability for material to resist bending, ratio of stress to strain	EI	EI = [Peak-Force*$Span^3$] ÷ [48*Displacement at Peak-Force]
Young's Modulus	MPa	measure of elasticity	EI/I	EI = [Peak-Force*Span^3] ÷ [48*Displacement at Peak-Force]
				I = moment of inertia (mm^4)

2.9 Statistical Analysis

Statistical analyses were accomplished using GraphPad Prism v.9.5.1. One-way analyses of variance (ANOVA) were performed to compare means between treatment groups (fentanyl, morphine, and control) for biomechanical, SRμCT, and cross-sectional geometric data. Alpha was set to $p<0.05$. Subsequent post-hoc tests (e.g., Tukey's and Holm-Šidák's multiple comparison) were performed to assess significance between groups. The following variables failed assumptions of normality: % pore volume, pore diameter, pore density, pore separation, lacunar separation, and lacunar density. Log-transformation was successful in normalizing % pore volume, pore diameter, and pore density. Thus, one-way ANOVAs were performed on these variables. However, log-transformation did not correct pore separation, lacunar separation, and lacunar density. Thus, non-parametric Kruskal-Wallis H-tests were performed on these variables.

To investigate the relationships between SRμCT, biomechanical, and cross-sectional geometric data, simple linear regression models and Pearson's R Correlation coefficient analyses were performed. Alpha was set to $p<0.05$.

3. Results

3.1 SRμCT Imaging Results

SRμCT imaging experiments allowed for the evaluation of microstructural features in our control, fentanyl, and morphine groups. The morphometric variables of interest, as well as their descriptive statistics are reported in **Table 3.** Morphometric variables were compared between groups to analyze differences between the treatment groups using one-way ANOVAs and Kruskal-Wallis H-tests, as well as subsequent post-hoc analysis to examine group relationships (**Table 4**).

One-way ANOVAs revealed that the morphine group demonstrated both larger pore diameter ($F(2, 20) = 4.809$, $p = 0.0243$), and a greater number of pores ($F(2, 20) = 4.191$, $p = 0.0331$) compared to the fentanyl group **(Figure 8 a. & b., Table 4)**. The morphine group further demonstrated a greater number of osteocyte lacunae compared to the control group ($F(2, 20) = 4.345$, $p = 0.0283$)(**Figure 8 c., Table 4)**. The fentanyl group, however, hosted a greater number of osteocyte lacunae compared to the control group, though not significantly so. Overall, these findings suggest that the morphine group demonstrated greater overall porosity compared to the fentanyl and control animals.

Table 3. *Descriptive statistics (mean and standard deviation (SD)) for SRμCT morphometric imaging variables of rabbit tibiae by treatment group.*

Morphometric Variable		Fentanyl		Control		Morphine	
		Mean	**SD**	**Mean**	**SD**	**Mean**	**SD**
Pore Data	% Pore Volume	1.4760	0.4176	1.4860	0.4780	1.6290	0.2501
	% Pore Surface	1.2190	0.1835	1.2390	0.2173	1.2490	0.2286
	Pore Surface/Volume Ratio (1/mm)	291.07	42.47	288.13	47.45	263.73	40.91
	Pore Surface Density (1/mm)	4.15	0.45	4.10	0.46	4.25	0.57
	Pore Diameter (mm)	***0.01674**	0.0037	0.0168	0.0016	***0.025005**	0.0078
	Pore Separation (mm)	0.1754	0.0101	0.1746	0.0080	0.1688	0.0137
	Pore Connectivity Density (1/mm)	0.00027	0.00006	0.00029	0.00008	0.00031	0.00013
	# Pores/mm3	***535.3**	278.7	594.1	141.4	***1279**	1046
Lacunar Data	% Lacunar Volume	2.1730	0.7392	1.9940	0.3725	2.1800	0.6433
	% Lacunar Surface	5.1090	0.6846	4.9560	0.6611	5.3470	1.3680
	Lacunar Surface/Volume Ratio (1/mm)	854.67	103.07	839.33	65.11	858.00	68.60
	Lacunar Surface Density (1/mm)	17.95	3.91	16.55	1.91	18.40	4.29
	Lacunar Diameter (mm)	0.0048	0.0008	0.0048	0.0006	0.0048	0.0006
	Lacunar Separation (mm)	0.0658	0.0221	0.0768	0.0046	0.0722	0.0032
	Lacunar Connectivity Density (1/mm)	0.0009	0.0005	0.0006	0.0002	0.0014	0.0012
	# Lacunae/mm3	42918	5520	***36457**	2404	***46595**	8631

Table 4. *ANOVA and non-parametric (Kruskal-Wallis) results for SRμCT morphometric imaging variables of right rabbit tibiae. Post-hoc multiple comparison test results included.*

Morphometric Variable		***One-way ANOVA***		***Kruskal-Wallis H-Test***		***Post-hoc multiple comparisons tests***		
		F	***p-value***	***Kruskal-Wallis Statistic***	***p-value***	***Tuckey's Honestly Significant Difference Test***	***Holm-Šidák's Test***	***Dunn's Multiple Comparison Test***
Pore Data	% Pore Volume	*0.5973*	*0.5615*	-	-	-	*F vs. C = -8.685e-005* *F vs. M = 0.05096* *M vs. C = 0.05104*	-
	% Pore Surface	*0.0348*	*0.9657*	-	-	-	*F vs. C = -0.01965* *F vs. M = -0.02920* *M vs. C = -0.00955*	-
	Pore Surface/Volume Ratio (1/mm)	*0.8193*	*0.4374*	-	-	*F vs. C = 2.88* *F vs. M = 27.30* *M vs. C = 24.42*	-	-
	Pore Surface Density (1/mm)	*0.1455*	*0.8657*	-	-	*F vs. C = 0.05339* *F vs. M = -0.09302* *C vs. M = -0.1464*	-	-
	Pore Diameter (mm)	***4.8090***	****0.0243***	-	-	*F vs. C =-0.006495* *F vs. M =-0.1620* *C vs. M = -0.1555*	-	-
	Pore Separation (mm)	-	-	*1.5970*	*0.4651*	-	-	*F vs. C = 0.9762* *F vs. M = 3.8700* *C vs. M = 2.8810*
	Pore Connectivity Density (1/mm)	*0.3361*	*0.7192*	-	-	*F vs. C =-1.995e-005* *F vs. M =-4.157e-005* *C vs. M =-2.162e-005*	-	-
	# Pores/mm3	***2.8010***	****0.0888***	-	-	-	*F vs. C =0.07223* *F vs. M =0.3210* *C vs. M =0.2488*	-
Lacunar Data	% Lacunar Volume	*0.1835*	*0.8339*	-	-	-	*F vs. C =0.1782* *F vs. M =-0.007610* *C vs. M =-0.1858*	-

	% Lacunar Surface	*0.2657*	*0.7698*	-	-	-	*F vs. C =0.1526* *F vs. M =-0.2377* *C vs. M =-0.3902*	-
	Lacunar Surface/Volume Ratio (1/mm)	*0.0954*	*0.9095*	-	-	*F vs. C =15.20* *F vs. M =-3.723* *C vs. M =-18.92*	-	-
	Lacunar Surface Density (1/mm)	*0.4570*	*0.6407*	-	-	*F vs. C =1.400* *F vs. M =-0.4527* *C vs. M =-18.92*	-	-
	Lacunar Diameter (mm)	*0.0225*	*0.9778*	-	-	-	*F vs. C =1.617e-005* *F vs. M =-5.557e-005* *C vs. M =-7.174e-005*	-
	Lacunar Separation (mm)	-	-	*1.9990*	*0.3810*	*F vs. C =-0.01097* *F vs. M = -0.006435* *C vs. M = 0.004536*	-	-
	Lacunar Connectivity Density (1/mm)	*1.5070*	*0.2514*	-	-	*F vs. C =0.1299* *F vs. M =-0.1287* *C vs. M =-0.2585*	-	-
	# Lacunae/mm3	***0.4345***	****0.0299***	-	-	*F vs. C =5.929* *F vs. M =-2.429* *C vs. M =-8.357*	-	-

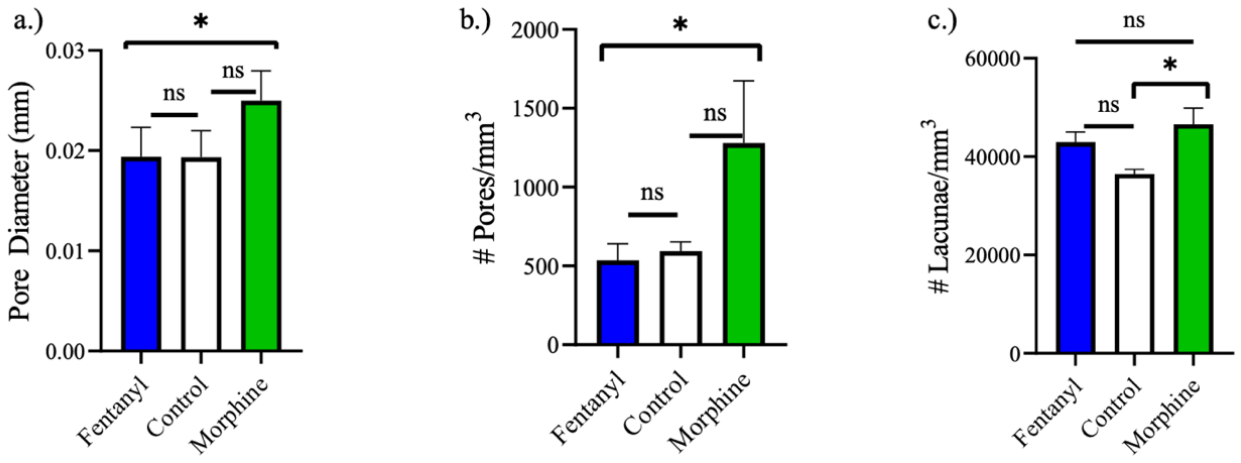

Figure 8. *Microstructural parameters with significant difference between groups (α = 0.05; * = p<0.05). a.) One-way ANOVA reflects significant differences between morphine and fentanyl groups comparing mean pore diameter (mm) b.) One-way ANOVA reflects significant differences between morphine and fentanyl groups comparing the number of objects. c.) Kruskal-Wallis H-Test reflects a significant difference between morphine and control group comparing number of objects.*

3.2 Cross-Sectional Geometric Results

Various cross-sectional geometric values for control, fentanyl, and morphine groups were obtained via BoneJ. The cross-sectional variables of interest, as well as their descriptive statistics are reported in **Table 5.** Cross-sectional variables were compared between groups to analyze differences between the treatment types using one-way ANOVAs (**Table 6**).

One-way ANOVAs revealed no significant differences between groups among the following variables: cortical area ($F(2,20) = 4.312$, $p = 0.6566$), perimeter ($F(2,20) = 1.988$, $p = 0.1675$), medullary area ($F(2,20) = 0.05343$, $p = 0.9481$), and moment of inertia ($F(2,20) = 0.1412$, $p = 0.2709$) **(Figure 9)**. It is observable that the morphine animals have marginally greater mean cross-sectional areas (mm^2) and perimeters (mm) than fentanyl and control groups.

Additionally, the fentanyl group demonstrates a greater moment of inertia (IML) compared to the control and morphine groups.

Table 5. *Descriptive statistics (mean and standard deviation (SD)) for cross-sectional geometric variables of right rabbit tibiae by treatment group.*

Cross-sectional Geometric Variables	Fentanyl		Control		Morphine	
	Mean	SD	Mean	SD	Mean	SD
Cortical Area (mm^2)	24.19	2.062	23.88	2.323	24.85	1.363
Medullary Area (mm^2)	13.72	3.342	13.17	4.053	13.66	2.389
Perimeter (mm)	232.6	7.24	230.9	5.572	237.3	5.2
Moment of Inertia (IML)	0.010 52	0.001 437	0.008 914	0.001 09	0.01	0.00 2346

Table 6. *ANOVA results for cross-sectional geometric variables of right rabbit tibiae. Post-hoc multiple comparison test results included.*

Cross-sectional Geometric Variables	***One-way ANOVA***		***Post-hoc multiple comparison test***
	F	***p-value***	***Holm-Šidák's Test***
Cortical Area (mm2)	0.4312	0.6566	*F vs. C = 0.3188* *F vs. M =-0.6512* *C vs. M =-0.9700*
Medullary Area (mm2)	0.05343	0.9481	*F vs. C = 0.5488* *F vs. M =0.05465* *C vs. M =-0.4942*
Perimeter (mm)	1.988	0.1675	*F vs. C = 1.694* *F vs. M = -4.737* *C vs. M = -6.431*
Moment of Inertia (IML)	1.412	0.2709	*F vs. C = 0.001602* *F vs. M = 0.0005127* *C vs. M =-0.001090*

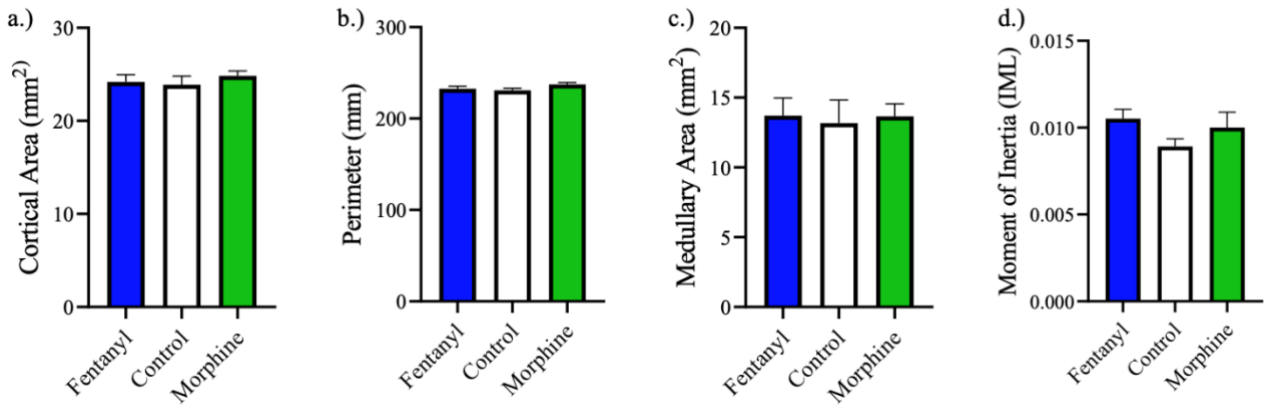

Figure 9. *Cross-sectional geometric parameters with significant difference between groups via one-way ANOVAs (α = 0.05; * = p<0.05). a.) No significant differences between control, morphine, and fentanyl groups comparing mean cross-sectional area (mm^2) b.) No significant differences between control, morphine and fentanyl groups comparing mean perimeter (mm). c.) No significant differences between control, morphine, and fentanyl groups comparing Medullary Area (mm^2). d.) No significant differences between control, morphine and fentanyl groups comparing moment of inertia (IML).*

3.3 Biomechanical Bend-Test Results

Raw 3-point bend-test data were collected to compare preliminary biomechanical data between treatment groups. Data exclusive to the loading region of the force-displacement curve were considered for this analysis because it is only within the loading region of the bend-test data produced that works to describe the sample's behaviour under loading (**Figure 7**). The biomechanical variables of interest (e.g., peak force, displacement, time, strength, flexural modulus, and young's modulus), as well as their descriptive statistics, are reported in **Table 7.**

Biomechanical variables were analyzed using one-way ANOVAs to examine differences between the treatments, as well as subsequent post-hoc analyses to examine any significant differences found (**Table 8**). One-way ANOVA analyses evaluating differences between groups demonstrated that there were no significant differences between control and drug groups across

peak force ($F(2,20) = 0.5805$, $p = 0.5703$), displacement ($F(2,20) = 1.634$, $p = 0.2244$), and time ($F(2,20) = 1.593$, $p = 0.2323$) (**Figure 10, a.-c.**). Visually, however, we can appreciate that the control group animal results indicate greater peak load (N), displacement (mm), and time (s).

Additional biomechanical variables of interest can be determined by using both 3-point bend test data and cross-sectional data to calculate more complex descriptors of biomechanical performance such as strength, flexural modulus, and young's modulus. Calculations and descriptions of these variables are presented in **Table 2**. These variables of interest, and their descriptive statistics, are reported in **Table 7**. Biomechanical variables were analyzed using one-way ANOVAs to examine differences between the treatment types, as well as subsequent post-hoc analyses to examine any significant differences found (**Figure 10, d.-f; Table 8**).

Descriptors of biomechanical performances were analyzed using one-way ANOVAs to reflect group differences. The results of these one-way ANOVAs demonstrated that there were no significant differences between control and drug groups for strength ($F(2,20) = 2.2474$, $p = 0.1140$), Flexural Modulus ($F(2,20) = 0.8290$, $p = 0.4534$), and Young's Modulus ($F(2,20) = 0.9935$, $p = 0.3908$) (**Figure 10**). Visually, however, the control group revealed the greatest strength (MPa) and young's modulus (MPa) compared to both drug groups. While trends are less obvious in this variable, it does appear that the fentanyl group has the greatest flexural modulus ($MPa*mm^4$) followed closely by the control group and the morphine group.

Table 7. *Descriptive statistics (mean and standard deviation (SD)) for biomechanical variables of rabbit tibiae by treatment group.*

Biomechanical Variable	Fentanyl		Control		Morphine	
	Mean	SD	Mean	SD	Mean	SD
Peak Force (N)	310.8	20.02	326.9	41.29	315	18.38
Displacement (mm)	1.589	0.1019	1.721	0.1568	1.64	0.1346
Time (s)	102.4	6.503	109.7	9.271	105.1	6.21
Strength (Mpa)	345.8	34.01	428.1	82.25	368.7	79.46
Flexural Modulus (Mpa*mm^4)	1517023	89545	1453421	197485	1410735	166840
Young's Modulus (Mpa)	14632	1958	16640	3850	14311	3534

Table 8. *ANOVA results for biomechanical variables of rabbit tibiae by treatment group. Post-hoc multiple comparison test results included.*

Biomechanical Variable	One-way ANOVA		***Post-hoc multiple comparison test***
	F	***p*-value**	***Holm-Šidák's Test***
Peak Force (N)	0.5805	0.5703	*F vs. C = -16.08* *F vs. M = -4.133* *C vs. M =11.95*
Displacement (mm)	1.634	0.2244	*F vs. C = -0.1317* *F vs. M = -0.05106* *C vs. M =0.08067*
Time (s)	1.593	0.2323	*F vs. C = -7.246* *F vs. M = -2.721* *C vs. M =4.525*
Strength (Mpa)	2.474	0.114	*F vs. C = -82.24* *F vs. M = -22.86* *C vs. M =59.39*
Flexural Modulus (Mpa*mm^4)	0.829	0.4534	*F vs. C = 63603* *F vs. M = 106288* *C vs. M =42686*

Young's Modulus (Mpa)	0.9935	0.3908	*F vs. C = -2008.0* *F vs. M = 320.4* *C vs. M =2329.0*

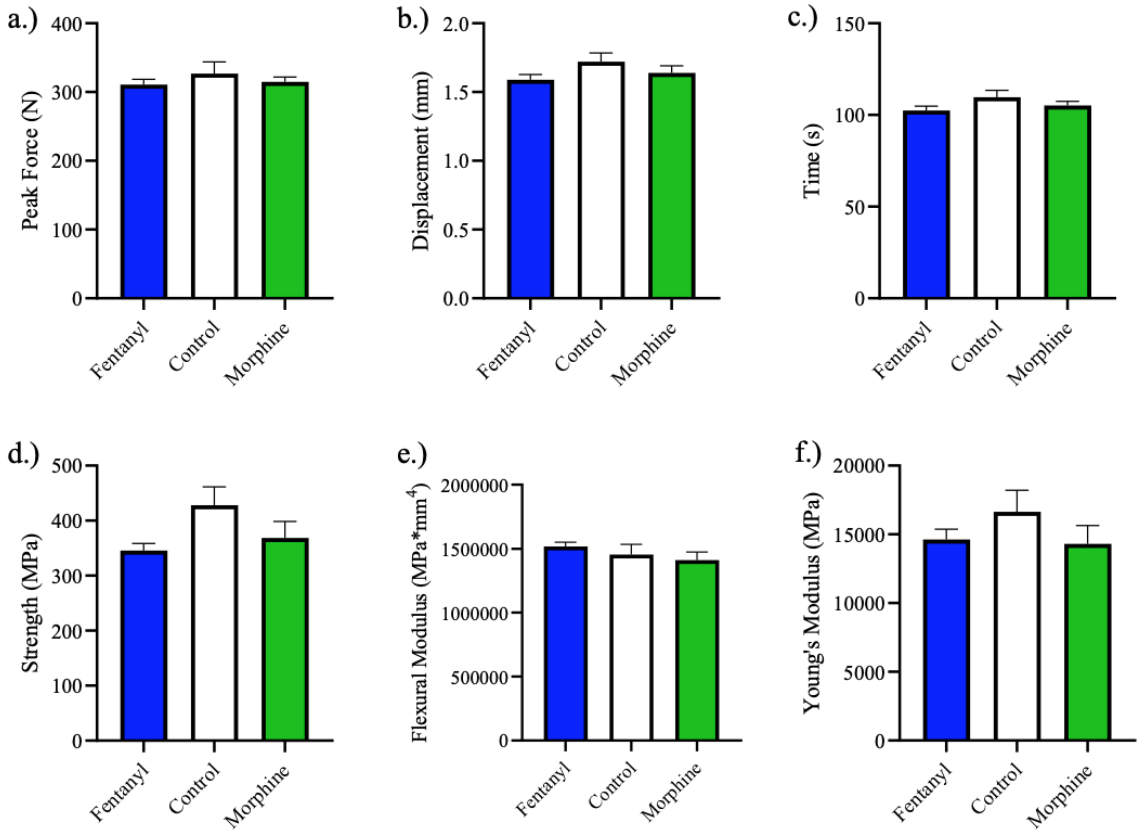

Figure 10. *Bar graphs displaying one-way ANOVA results of treatment group difference between biomechanical variables, α = 0.05. a.) No significant differences between control, morphine, and fentanyl groups comparing peak force (N). b.) No significant differences between control, morphine, and fentanyl groups comparing mean displacement (mm). c.) No significant differences between control, morphine, and fentanyl groups comparing mean test time (s). d.) No significant differences between control, morphine, and fentanyl groups comparing mean strength (MPa). e.) No significant differences between control, morphine, and fentanyl groups comparing Flexural Modulus (MPa*mm^4). f.) No significant differences between control, morphine, and fentanyl groups comparing mean (MPa).*

3.4 Correlation Analysis

The Control Group

Pearson's correlation coefficient analyses were computed to further examine the relationship between the control, morphine, and fentanyl group's SRμCT imaging parameters, cross-sectional geometric properties, and biomechanical parameters. The control group's correlation coefficients indicated which variables shared significant relationships at $\alpha \leq 0.05$ **(Tables 9 and 10, Figure 11).** Significant positive linear correlations were observed between peak force and % pore volume (r = 0.8332), pore diameter (r = 0.8468), and cortical area (r = 0.8188); and between cortical area and % pore volume (r = 0.8614), % pore surface (r = 0.8766), and pore diameter (r = 0.9027). Significant negative linear correlations were observed between peak force and pore surface/volume ratio (r =-0.9039); between strength and lacunar density (r = -0.8694); and between cortical area and pore surface/volume ratio (r = -0.8432). Spearman's rank correlation analysis was performed to examine the relationship between lacunar separation (non-parametric as this variable is not homogeneous) and peak force and determined there is a significant positive linear correlation (r = 0.8857) (**Table 10**).

Table 9. Pearson's Correlation Coefficient Control Group Results. $\alpha \leq 0.05$. * Indicates p-value ≤ 0.05. ** indicates p-value ≤ 0.01.

		Peak Force (N)	Displacement (mm)	Time (s)	Strength (Mpa)	Flexural Modulus	Young's Modulus (Mpa)	Cortical Area (mm2)	Perimeter (mm)	Medullary Area (mm2)	Moment of Inertia
% Pore Volume	*r*	0.8332	0.2669	-0.3351	0.2784	0.4993	0.1380	0.8624	0.6825	0.6774	0.2430
	R2	0.6942	0.0712	0.1123	0.0775	0.2493	0.0191	0.7420	0.4658	0.4588	0.0590
	p	***0.0394**	0.6092	0.5161	0.5931	0.3133	0.7943	***0.0275**	0.1352	0.1393	0.6427

% Pore Surface	*r*	0.7765	-0.1659	-0.2462	0.0616	0.2784	-0.0962	0.8766	0.5793	0.7658	0.4007
	R2	0.6030	0.0275	0.0606	0.0038	0.0775	0.0093	0.7685	0.3356	0.5865	0.1606
	p	0.0693	0.7535	0.6382	0.9077	0.5932	0.8562	***0.0219**	0.2282	0.0758	0.4311
Pore Surface/ Volume Ratio (1/mm)	*r*	-0.9039	0.4332	0.4781	-0.4859	-0.6824	-0.3633	-0.8432	-0.7229	-0.6168	-0.0355
	R2	0.8170	0.1877	0.2286	0.2361	0.4657	0.1320	0.7110	0.5225	0.3805	0.0013
	p	***0.0134**	0.3908	0.3375	0.3285	0.1353	0.4791	***0.0349**	0.1046	0.1921	0.9467
Pore Surface Density	*r*	0.6533	-0.1795	-0.3019	0.0898	0.2680	-0.0868	0.6362	0.5377	0.4456	0.4489
	R2	0.4267	0.0322	0.0912	0.0081	0.0718	0.0075	0.4047	0.2891	0.1986	0.2016
	p	0.1595	0.7336	0.5609	0.8656	0.6076	0.8701	0.1745	0.2712	0.3758	0.3718
Pore Diameter (mm)	*r*	0.8468	-0.2530	-0.3086	0.2714	0.4884	0.1378	0.9027	0.6621	0.7494	0.2135
	R2	0.7170	0.0640	0.0952	0.0737	0.2385	0.0190	0.8149	0.4383	0.5616	0.0456
	p	***0.0334**	0.6285	0.5518	0.6029	0.3257	0.7946	***0.0137**	0.1520	0.0863	0.6846
Pore Connectivity Density (1/mm)	*r*	-0.4759	0.6887	0.7651	-0.6738	-0.6410	-0.5692	-0.0092	-0.3605	0.3391	0.2354
	R2	0.2265	0.4744	0.5854	0.4541	0.4109	0.3240	0.0001	0.1299	0.1150	0.0554
	p	0.3401	0.1302	0.0763	0.1422	0.1702	0.2384	0.9.862	0.4827	0.5108	0.6534
# Pores/mm3	*r*	-0.1803	0.2608	0.1765	-0.6455	-0.7380	-0.7525	-0.0740	-0.4318	0.1253	0.5246
	R2	0.0325	0.0680	0.0312	0.4167	0.5447	0.5663	0.0055	0.1865	0.0157	0.2752
	p	0.7325	0.6176	0.7379	0.1662	0.0939	0.0843	0.8892	0.1865	0.8130	0.2853

% Lacunar Volume	*r*	0.0029	-0.3687	-0.3930	-0.0237	-0.3171	-0.1072	-0.2760	-0.5518	-0.1568	-0.1871
	R2	0.0000	0.1360	0.1545	0.0006	0.1006	0.0115	0.0762	0.3045	0.0246	0.0350
	p	0.9956	0.4720	0.4408	0.9644	0.5402	0.8398	0.5965	0.2563	0.7668	0.7226
% Lacunar Surface	*r*	0.3278	-0.2893	-0.3054	-0.1148	-0.2367	-0.2215	0.2690	-0.2386	0.4154	0.0186
	R2	0.1074	0.0837	0.0933	0.0132	0.0560	0.0491	0.0724	0.0569	0.1725	0.0003
	p	0.5260	0.5781	0.5561	0.8286	0.6516	0.6732	0.6063	0.6489	0.4128	0.9720
Lacunar Surface/ Volume Ratio (1/mm)	*r*	-0.1070	0.5263	0.5627	-0.2157	0.1387	-0.1090	0.3120	0.5459	0.2567	0.3494
	R2	0.0115	0.2770	0.3167	0.0465	0.0192	0.0119	0.0973	0.2980	0.0659	0.1221
	p	0.8401	0.2834	0.2450	0.6814	0.7933	0.8372	0.5472	0.2625	0.6233	0.4972
Lacunar Surface Density	*r*	-0.0669	-0.2402	-0.2616	-0.1739	-0.4269	-0.2456	-0.2512	-0.5507	-0.0950	-0.0697
	R2	0.0045	0.0577	0.0685	0.0303	0.1822	0.0603	0.0631	0.3033	0.0090	0.0049
	p	0.8997	0.6467	0.6165	0.7417	0.3986	0.6390	0.6311	0.2575	0.8580	0.8956
Lacunar Diameter (mm)	*r*	0.0178	-0.4470	-0.4767	0.1687	-0.2178	0.0732	-0.3794	-0.6475	-0.2810	-0.3670
	R2	0.0003	0.1998	0.2273	0.0285	0.0474	0.0054	0.1440	0.4192	0.0790	0.1347
	p	0.9733	0.3742	0.3391	0.7494	0.6784	0.8904	0.4582	0.1645	0.5896	0.4742
Lacunar Connectivity Density	*r*	-0.6413	0.6173	0.7741	-0.0869	-0.6314	-0.7806	-0.1814	0.0173	-0.0701	0.7365
	R2	0.4113	0.6173	0.5993	0.7559	0.3987	0.6093	0.0329	0.0003	0.0049	0.5424
	p	0.1699	0.0640	0.0708	***0.0245**	0.1787	0.0669	0.7308	0.9741	0.8950	0.0950

# Lacunae/mm3	*r*	-0.4470	0.6013	0.6367	-0.7597	-0.7950	-0.7154	-0.0612	-0.4953	0.3029	0.3325
	R2	0.1998	0.3616	0.4054	0.5772	0.6320	0.5118	0.0037	0.2453	0.0917	0.1105
	p	0.3742	0.2067	0.1740	0.0797	0.0587	0.1100	0.9083	0.3178	0.5596	0.5197
Cortical Area (mm2)	*r*	0.8188	-0.1969	-0.2036	0.1713	0.4467	0.0882				
	R2	0.6705	0.0388	0.0415	0.0293	0.1995	0.0078				
	p	***0.0463**	0.7084	0.6988	0.0746	0.3745	0.8681				
Perimeter (mm)	*r*	0.6154	-0.2562	-0.2761	0.2808	0.6815	0.2583				
	R2	0.3787	0.0656	0.0762	0.0788	0.4645	0.0667				
	p	0.1934	0.6241	0.5964	0.5899	0.1360	0.6211				
Medullary Area (mm2)	*r*	0.6162	0.0405	0.0542	-0.0644	0.1261	-0.1299				
	R2	0.3797	0.0016	0.0029	0.0041	0.0159	0.0169				
	p	0.1927	0.9392	0.9187	0.9035	0.8119	0.8063				
Moment of Inertia	*r*	-0.2084	0.6524	0.5487							
	R2	0.0434	0.4256	0.3011							
	p	0.6919	0.1603	0.2595							

Table 10. Spearman's Rank Correlation results of control group's nonparametric variables. $\alpha \leq 0.05$. * Indicates p-value ≤ 0.05. ** indicates p-value ≤ 0.01.

		Peak Force (N)	Displacement (mm)	Time (s)	Strength (Mpa)	Flexural Modulus (Mpa*mm3)	Young's Modulus (Mpa)	Cortical Area (mm2)	Perimeter (mm)	Medullary Area (mm2)	Moment of Inertia
Pore Separation (mm)	*r*	0.2000	0.2000	0.3714	0.0857	0.2000	0.0857	0.6571	0.6000	0.7714	0.0286
	p	0.7139	0.7139	0.4972	0.9194	0.7139	0.9194	0.1750	0.2417	0.1028	>0.9999
Lacunar Separation (mm)	*r*	0.8857	-0.7143	-0.6000	0.8286	0.7714	0.8286	0.6000	0.4857	0.2571	-0.6571
	p	***0.0333*** *	0.1361	0.2417	0.0583	0.1028	0.0583	0.2417	0.3556	0.6583	0.1750

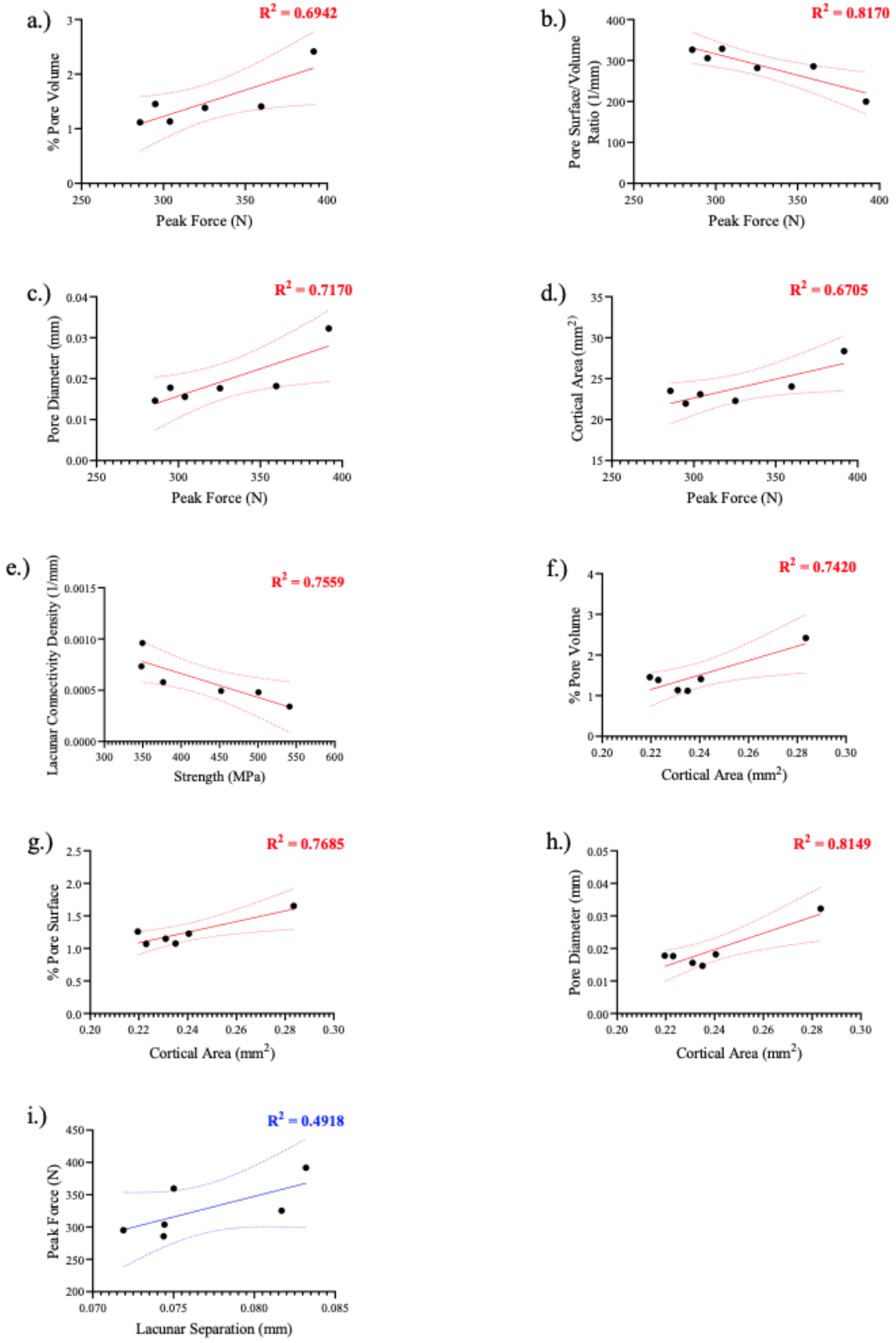

Figure 11. Simple linear regression plots demonstrating significant trends in the control group.

The Fentanyl Group

Correlation coefficients indicated which variables shared significant relationships at $\alpha \leq 0.05$ **(Tables 11 and 12, Figure 12).** Significant positive linear correlations were observed between peak force and lacunar surface/volume ratio (r = 0.8400); between flexural modulus and % pore volume (r = 0.9130), and pore surface density (r = 0.9086); between cortical area and % pore surface (r = 0.9354), and lacunar surface to volume ratio (r = 0.8506); between moment of inertia and % pore surface (r = 0.8530); between medullary area and % pore surface (r = 0.7936), lacunar surface to volume ratio (r = 0.8111). Spearman's rank correlation analysis was performed to examine the relationship between lacunar separation (non-parametric as this variable is not homogeneous) cortical (r = 0.7857) and medullary (r = 0.8313) area and determined there is a significant positive linear correlation (**Table 12**).

Significant negative linear correlations were observed between peak force and % lacunar volume (r = -0.7980), % lacunar surface (r = -0.7578), and lacunar diameter (r = 0.8163); between flexural and pore separation (r = 0.8029); between strength and perimeter (r = -0.7939); between young's modulus and perimeter (r = -0.8091); between cortical area and % lacunar volume (r = -0.8383), lacunar surface density (r = -0.8065), and lacunar diameter (r = -0.8546). Additional significant negative linear correlations include correlations between perimeter and pore connectivity density (r = -0.8981), between medullary area and % pore surface (r = -0.7936), % lacunar volume (r = -0.9199), lacunar surface density (r = -0.9403), lacunar diameter (r = -0.8119), and number of lacunae/mm^3 (r = -0.8668).

Table 11. Pearson's Correlation Coefficient Fentanyl Group Results. $\alpha \leq 0.05$. * Indicates p-value ≤ 0.05. ** indicates p-value ≤ 0.01.

		Peak Force (N)	Displacement (mm)	Time (s)	Strength (Mpa)	Flexural Modulus (Mpa*mm4)	Young's Modulus (Mpa)	Cortical Area (mm2)	Perimeter (mm)	Medullary Area (mm2)	Moment of Inertia
% Pore Volume	*r*	0.4005	0.4680	0.4579	0.1545	0.9130	-0.1242	0.0401	0.1776	-0.1658	0.5033
	R2	0.1604	0.2191	0.2097	0.0239	0.8335	0.0154	0.0016	0.0315	0.0275	0.2533
	p	0.3733	0.2895	0.3015	0.7409	***0.0041*** **	0.7908	0.9320	0.7033	0.7224	0.2495
% Pore Surface	*r*	0.6878	0.0979	0.1290	-0.5877	0.3051	-0.7062	0.9354	0.2532	0.7936	0.8530
	R2	0.4730	0.0096	0.0167	0.3454	0.0931	0.4987	0.8750	0.0641	0.6299	0.7275
	p	0.0877	0.8347	0.7828	0.1652	0.5058	0.0761	***0.0020*** **	0.5839	***0.0331*** *	***0.0147****
Pore Surface/ Volume Ratio (1/mm)	*r*	-0.1470	-0.3046	-0.2938	0.0245	-0.7317	0.2658	0.0447	-0.4647	0.3423	-0.5506
	R2	0.0216	0.0928	0.0863	0.0006	0.5354	0.0707	0.0020	0.2160	0.1171	0.3032
	p	0.7532	0.5065	0.5225	0.9584	0.0616	0.5645	0.9242	0.2934	0.4524	0.2002
Pore Surface Density	*r*	0.6067	0.5391	0.5351	0.2721	0.9.86	0.0234	0.2125	-0.1634	0.1435	0.4046
	R2	0.3681	0.2906	0.2863	0.0740	0.8256	0.0005	0.0414	0.0267	0.0206	0.1637
	p	0.1486	0.2118	0.2159	0.5550	***0.0046*** **	0.9603	0.6474	0.7263	0.7590	0.3679
Pore Diameter (mm)	*r*	0.0187	0.3996	0.3895	0.0994	0.6932	-0.1213	-0.2442	0.4073	-0.5062	0.3627
	R2	0.0003	0.1597	0.1517	0.0099	0.4805	0.0147	0.0596	0.1659	0.2563	0.1315
	p	0.9683	0.3744	0.3877	0.8321	0.0842	0.7956	0.5977	0.3645	0.2463	0.4240

Pore Separation (mm)	*r*	-0.2504	-0.7452	-0.7380	-0.6174	-0.8029	-0.4405	0.2636	0.3564	0.2282	0.0761
	R2	0.0627	0.5553	0.5446	0.3812	0.6446	0.1940	0.0695	0.1270	0.0521	0.0058
	p	0.5881	0.0546	0.0583	0.1396	***0.0296****	0.3226	0.5678	0.4326	0.6226	0.8712
Pore Connectivity Density (1/mm)	*r*	0.3493	-0.0298	-0.0453	0.5393	-0.0496	0.5826	-0.0348	-0.8981	0.3317	-0.5583
	R2	0.1220	0.0009	0.0021	0.2909	0.0025	0.3394	0.0012	0.8065	0.1101	0.3117
	p	0.4425	0.9495	0.9231	0.2115	0.9159	0.1699	0.9410	***0.006****	0.4673	0.1927
# Pores/mm3	*r*	-0.1207	-0.1163	-0.1625	0.6225	0.1438	0.6233	-0.4185	-0.4800	-0.2717	-0.4400
	R2	0.0146	0.0135	0.0264	0.3875	0.0207	0.3885	0.1752	0.2304	0.0738	0.1936
	p	0.7966	0.8040	0.7277	0.1355	0.7584	0.1348	0.3500	0.2757	0.5557	0.3232
% Lacunar Volume	*r*	-0.7980	-0.0443	-0.0803	0.3447	-0.0762	0.3926	-0.8383	0.2164	-0.9199	-0.4169
	R2	0.6368	0.0020	0.0065	0.1188	0.0058	0.1541	0.7028	0.0468	0.8462	0.1738
	p	0.0315	0.9248	0.8641	0.4490	0.8710	0.3837	***0.0185****	0.6412	***0.0033****	0.3521
% Lacunar Surface	*r*	-0.7578	-0.3409	-0.3494	-0.3220	-0.3557	-0.2414	-0.3789	0.7443	-0.6392	0.0721
	R2	0.5742	0.1162	0.1221	0.1037	0.1265	0.0583	0.1436	0.5540	0.4086	0.0052
	p	***0.0484****	0.4542	0.4424	0.4813	0.4336	0.6021	0.4019	0.0550	0.1222	0.8779
Lacunar Surface/ Volume Ratio (1/mm)	*r*	0.8400	-0.0810	-0.0316	-0.4929	0.0800	-0.5769	0.8506	0.0258	0.8111	0.5820
	R2	0.7055	0.0066	0.0010	0.2429	0.0064	0.3328	0.7235	0.0007	0.6579	0.3387
	p	***0.018****	0.8629	0.9463	0.2611	0.8647	0.1751	***0.0153****	0.9562	***0.0268****	0.1704

Lacunar Surface Density	*r*	-0.6976	-0.0171	-0.0463	0.3137	0.0281	0.3173	-0.8065	0.2888	-0.9403	-0.3096
	R2	0.4866	0.0003	0.0021	0.0984	0.0008	0.1007	0.6505	0.0834	0.8842	0.0958
	p	0.0814	0.9710	0.9215	0.4932	0.9522	0.4880	***0.0284****	0.5299	***0.0016****	0.4993
Lacunar Diameter (mm)	*r*	-0.8163	0.1234	0.0730	0.5209	-0.0311	0.5927	-0.8546	-0.0462	-0.8119	-0.5785
	R2	0.6640	0.0152	0.0053	0.2714	0.0010	0.3512	0.7303	0.0021	0.6592	0.3346
	p	***0.0251****	0.7922	0.8765	0.2306	0.9472	0.1608	***0.0143****	0.9216	***0.0265****	0.1737
Lacunar Connectivity Density	*r*	0.1011	-0.3722	-0.4154	0.5777	0.1145	0.5386	-0.3588	-0.4892	-0.2279	-0.3919
	R2	0.0102	0.1385	0.1726	0.3337	0.0131	0.2904	0.1287	0.2393	0.0520	0.1536
	p	0.8292	0.4110	0.3540	0.1744	0.8068	0.2120	0.4293	0.2652	0.6230	0.3846
# Lacunae/mm3	*r*	-0.3573	-0.0782	-0.1041	0.3548	0.2692	0.2601	-0.6866	0.2491	-0.8668	-0.1341
	R2	0.1277	0.0061	0.0108	0.1259	0.0747	0.0677	0.4714	0.0620	0.7513	0.0180
	p	0.4314	0.8676	0.8243	0.4349	0.5594	0.5732	0.0885	0.5902	***0.0116****	0.7744
Cortical Area (mm2)	*r*	0.6205	0.0624	0.1035	-0.6987	0.0693	-0.7453				
	R2	0.3851	0.0039	0.0107	0.4882	0.0048	0.5555				
	p	0.1370	0.8942	0.8253	0.0807	0.8827	0.0545				
Perimeter (mm)	*r*	-0.2405	-0.2949	-0.2699	-0.7939	-0.1908	-0.8091				
	R2	0.0579	0.0870	0.0728	0.6302	0.0364	0.6547				
	p	0.6033	0.5208	0.5583	0.0330	0.6820	0.0275				

Medullary Area (mm2)	*r*	0.6153	0.1544	0.1856	-0.4339	0.0179	-0.4300				
	R2	0.3785	0.0238	0.0344	0.1883	0.0003	-0.1849				
	p	0.1414	0.7410	0.6904	0.3307	0.9697	0.3356				
Moment of Inertia	*r*	0.4783	0.0552	0.0872							
	R2	0.2288	0.0030	0.0076							
	p	0.2776	0.9065	0.8525							

Table 12. Spearman's Rank Correlation results of fentanyl group's nonparametric variables. $\alpha \leq 0.05$. * Indicates p-value ≤ 0.05. ** indicates p-value ≤ 0.01.

		Peak Force (N)	**Displacement (mm)**	**Time (s)**	**Strength (Mpa)**	**Flexural Modulus (Mpa*mm3)**	**Young's Modulus (Mpa)**	**Cortical Area (mm2)**	**Perimeter (mm)**	**Medullary Area (mm2)**	**Moment of Inertia**
Lacunar Separation (mm)	r	0.3214	0.0000	0.0000	-0.3571	0.0714	-0.3571	0.7857	-0.1786	0.8313	0.0689
	p	0.4976	>0.9999	>0.9999	0.4444	0.9063	0.4444	**0.048***	0.7131	***0.0204****	0.8833

Figure 12. Simple linear regression plots demonstrating significant trends in the fentanyl group. Red trends indicate parametric assessment, blue trends indicate non-parametric assessment.

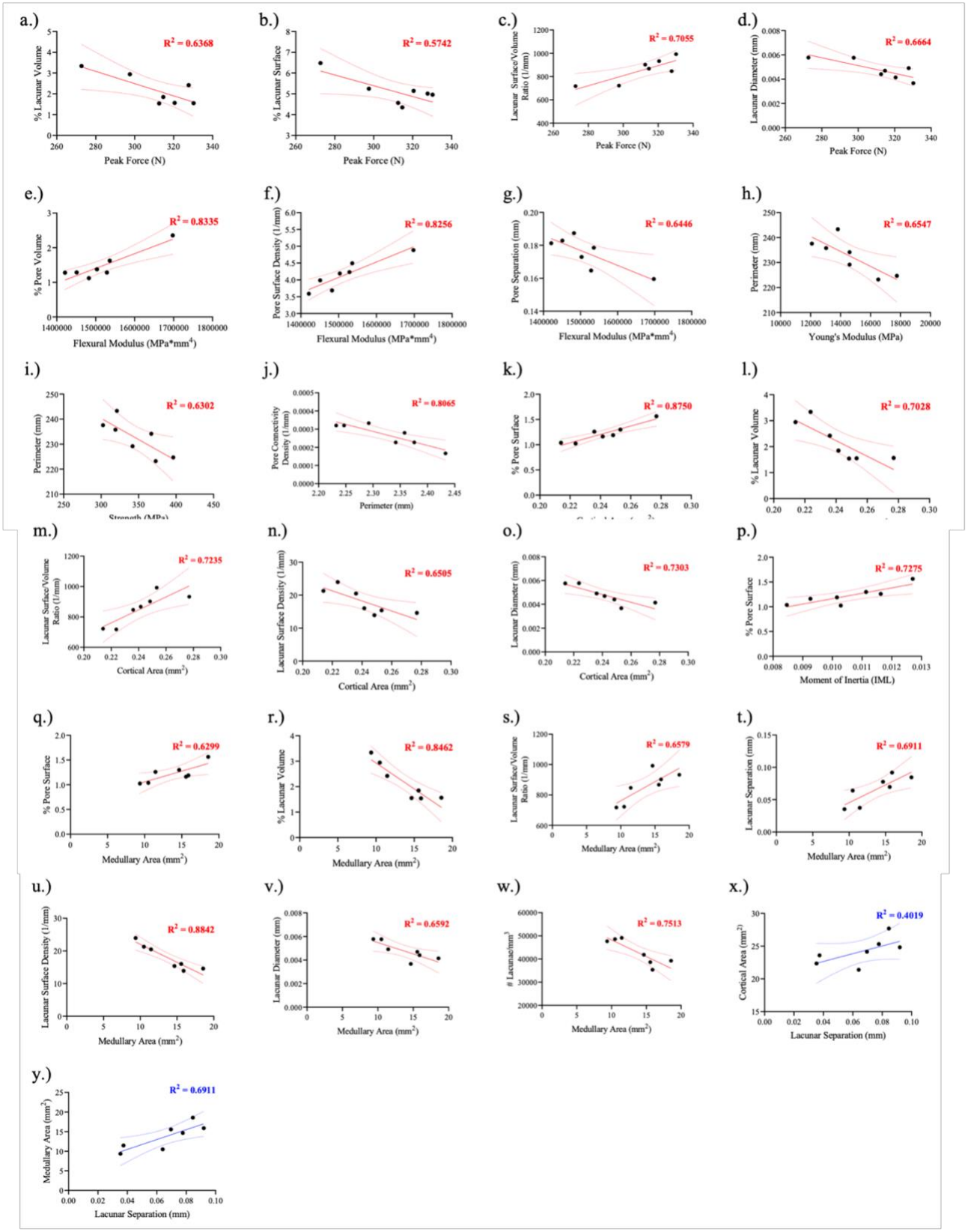

The Morphine Group

Correlation coefficients indicated which variables shared significant relationships at $\alpha \leq 0.05$ **(Table 13 and 14, Figure 13).** Significant positive linear correlations were observed between peak force and cortical area (r = 0.7754); between flexural modulus and number of pores/mm^3 (r = 0.7685) and lacunar connectivity density (r = 0.7635); and between medullary area and pore connectivity density (r = 0.7612). Significant negative linear correlations were observed between strength and moment of inertia (r = -0.9056), and between young's modulus and perimeter (r = -0.7963), and moment of inertia (r = -0.8990).

Table 13. Pearson's Correlation Coefficient Morphine Group Results. $\alpha \leq 0.05$. * Indicates p-value ≤ 0.05. ** indicates p-value ≤ 0.01.

		Peak Force (N)	Displacement (mm)	Time (s)	Strength (Mpa)	Flexural Modulus (Mpa*mm3)	Young's Modulus (Mpa)	Cortical Area (mm2)	Perimeter (mm)	Medullary Area (mm2)	Moment of Inertia
% Pore Volume	*r*	-0.3493	0.1821	0.2361	0.7089	0.0553	0.6089	-0.1303	-0.5658	0.1889	-0.3995
	R2	0.1220	0.0332	0.0558	0.5026	0.0031	0.3707	0.0168	0.3201	0.0357	0.1596
	p	0.4425	0.6959	0.6102	0.0745	0.9062	0.1467	0.7810	0.1855	0.6850	0.3746
% Pore Surface	*r*	0.1771	0.1251	0.2476	0.5776	0.3116	0.5512	0.0185	-0.6925	0.5411	-0.3504
	R2	0.0314	0.0156	0.0613	0.3337	0.0971	0.3038	0.0003	0.4795	0.2928	0.1228
	p	0.7040	0.7893	0.5924	0.1744	0.4964	0.1997	0.9687	0.0847	0.2097	0.4409
Pore Surface/Volu	*r*	0.5800	0.0203	0.0763	-0.2284	0.1634	-0.1731	0.2116	0.0095	0.5610	0.1329

me Ratio (1/mm)	*R2*	0.3364	0.0004	0.0058	0.0522	0.0267	0.0300	0.0448	0.0001	0.1303	0.0177
	p	0.1723	0.9656	0.8708	0.6223	0.7262	0.7105	0.6488	0.9839	0.4263	0.7764
Pore Surface Density	*r*	0.2152	0.1474	0.2656	0.4937	0.3612	0.4971	0.1005	-0.6720	0.6043	-0.2632
	R2	0.0463	0.0273	0.0705	0.2437	0.1305	0.2471	0.0101	0.4516	0.3652	0.0693
	p	0.6431	0.7525	0.5649	0.2602	0.4260	0.2564	0.8302	0.0982	0.1506	0.5685
Pore Diameter (mm)	*r*	-0.1912	0.3429	0.2855	0.0531	-0.0904	-0.0255	0.2920	0.0791	0.1767	0.2053
	R2	0.0366	0.1176	0.0815	0.0028	0.0082	0.0007	0.0853	0.0063	0.0312	0.0422
	p	0.6813	0.4515	0.5348	0.9100	0.8471	0.9567	0.5251	0.8662	0.7047	0.6587
Pore Separation (mm)	*r*	-0.1078	0.2601	0.1681	-0.1053	-0.7042	-0.3280	-0.0657	0.6987	-0.4120	0.0325
	R2	0.0116	0.0677	0.0283	0.0111	0.4959	0.1076	0.0043	0.4881	0.1698	0.0011
	p	0.8180	0.5732	0.7186	0.8223	0.0773	0.4727	0.8888	0.0808	0.3584	0.9449
Pore Connectivity Density (1/mm)	*r*	0.4566	0.2119	0.2988	0.0379	0.4460	0.1348	0.4109	-0.4099	0.7612	0.1282
	R2	0.2085	0.0449	0.0893	0.0014	0.1989	0.0182	0.1688	0.1681	0.5795	0.0165
	p	0.3030	0.6482	0.5151	0.9357	0.3158	0.7732	0.3598	0.3610	***0.0468****	0.7841
# Pores/mm3	*r*	0.2013	-0.2678	-0.2218	-0.1322	0.7685	0.1027	0.2716	-0.5305	0.4578	0.2298
	R2	0.0405	0.0717	0.0492	0.0175	0.5907	0.0105	0.0738	0.2814	0.2096	0.0528
	p	0.6652	0.5615	0.6327	0.7775	***0.0435****	0.8267	0.5557	0.2206	0.3016	0.6201
% Lacunar Volume	*r*	0.4455	0.1718	0.2413	0.0547	0.1251	0.1224	0.1242	-0.0154	0.3335	-0.1786

	R 2	0.1985	0.0295	0.0582	0.0030	0.0157	0.0150	0.0154	0.0002	0.1112	0.0319
	p	0.3164	0.7126	0.6022	0.9073	0.7892	0.7938	0.7908	0.9739	0.4648	0.0170
% Lacunar Surface	*r*	0.4588	0.2059	0.2895	0.0891	0.0731	0.1148	0.1194	-0.0838	0.3916	-0.1558
	R 2	0.2105	0.0424	0.0838	0.0079	0.0053	0.0132	0.0143	0.0070	0.1534	0.0243
	p	0.3004	0.6579	0.5288	0.8493	0.8762	0.8063	0.7987	0.8582	0.3849	0.7387
Lacunar Surface/Volume Ratio (1/mm)	*r*	-0.2629	0.0569	-0.0173	-0.4368	-0.4750	-0.5727	0.0320	0.3111	-0.2353	0.5557
	R 2	0.0691	0.0032	0.0003	0.1908	0.2256	0.3279	0.0010	0.0968	0.0554	0.3087
	p	0.5690	0.9036	0.9706	0.3271	0.2815	0.1790	0.9456	0.4971	0.6115	0.1953
Lacunar Surface Density	*r*	0.4668	0.2009	0.2670	-0.0491	0.0362	-0.0025	0.1477	0.0449	0.3361	-0.0677
	R 2	0.2179	0.0404	0.0713	0.0024	0.0013	0.0000	0.0218	0.0020	0.1129	0.0046
	p	0.2910	0.6658	0.5626	0.9168	0.9385	0.9958	0.7520	0.9239	0.4611	0.8853
Lacunar Diameter (mm)	*r*	0.2706	-0.0734	0.0073	0.3897	0.5137	0.5465	-0.0129	-0.3553	0.2745	-0.4997
	R 2	0.0732	0.0054	0.0000	0.1519	0.2639	0.2987	0.0002	0.1262	0.0754	0.2497
	p	0.5573	0.8757	0.9876	0.3875	0.2383	0.2043	0.9782	0.4342	0.5513	0.2335
Lacunar Connectivity Density	*r*	0.1791	-0.0657	-0.0260	-0.0746	0.7635	0.6218	0.4078	-0.5092	0.5983	0.2416
	R 2	0.0321	0.0043	0.0007	0.0056	0.5829	0.3867	0.1663	0.2593	0.3580	0.0584
	p	0.7008	0.8887	0.9559	0.8737	***0.0458****	0.1360	0.3637	0.2432	0.1559	0.6017
# Lacunae/mm 3	*r*	0.1579	0.0122	0.0844	-0.2054	0.1883	-0.0146	0.0400	-0.1559	0.2259	0.0719

	R2	0.0249	0.0001	0.0071	0.0422	0.0355	0.0002	0.0016	0.0243	0.0510	0.0052
	p	0.7353	0.9794	0.8573	0.6587	0.6860	0.9752	0.9322	0.7385	0.6262	0.8783
Cortical Area (mm2)	*r*	0.7754	0.6883	0.6338	-0.5383	0.0331	-0.5706				
	R2	0.6013	0.4737	0.4018	0.2897	0.0019	0.3256				
	p	***0.0405****	0.0873	0.1264	0.2126	0.9439	0.1810				
Perimeter (mm)	*r*	0.5150	0.4817	0.3719	-0.6342	-0.5439	-0.7963				
	R2	0.2653	0.2320	0.1383	0.4022	0.2959	0.6341				
	p	0.2368	0.2737	0.4114	0.1261	0.2069	***0.0321****				
Medullary Area (mm2)	*r*	0.7098	0.7154	0.7379	-0.1323	0.1124	-0.1913				
	R2	0.5038	0.5119	0.5445	0.0175	0.0126	0.0366				
	p	0.0740	0.0707	0.0583	0.7773	0.8105	0.6812				
Moment of Inertia	*r*	0.4263	0.3686	0.2923							
	R2	0.1818	0.1358	0.0855							
	p	0.3402	0.4159	0.5246							

Table 14. Spearman's Rank Correlation results of morphine group's nonparametric variables. α ≤ 0.05. * Indicates p-value ≤ 0.05. ** indicates p-value ≤ 0.01.

		Peak Force (N)	Displacement (mm)	Time (s)	Strength (Mpa)	Flexural Modulus	Young's Modulus (Mpa) (Mpa*mm3)	Cortical Area (mm2)	Perimeter (mm)	Medullary Area (mm2)	Moment of Inertia
Lacunar Separation (mm)	r	-0.1429	0.0000	0.0000	0.6786	0.3571	0.5357	-0.1071	-0.6071	0.1786	-0.2143
	p	0.7825	>0.9999	>0.9999	0.1095	0.4444	0.2357	0.8397	0.1667	0.7131	0.6615

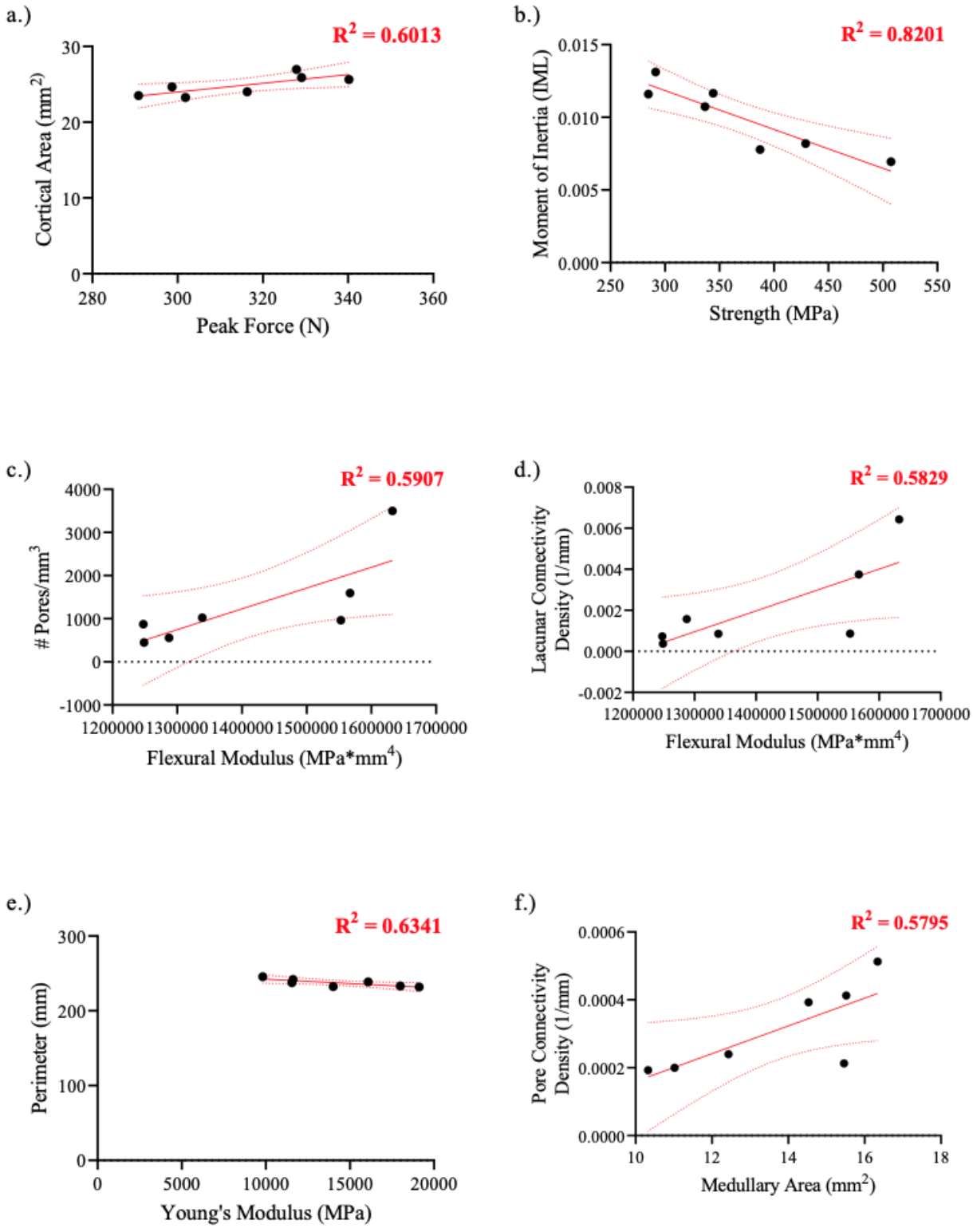

Figure 13. Simple linear regression plots demonstrating significant trends in the morphine group.

4. Discussion.

4.1 SRμCT Imaging Data

Current literature suggests that opioids dysregulate the key endocrine regulators of bone remodelling, as well as reduce osteoblastic activity, creating a decrease in bone density [7,37,38,41–43,45–48]. Consequently, we hypothesized that a decreased lacunar density and increased cortical porosity in opioid animals compared to control groups. However, some interesting trends emerged. The morphine group demonstrated the greatest overall porosity compared to fentanyl and control animals. The morphine group demonstrated the greatest pore diameter and number of pores (M>C>F) but was only significantly different from the fentanyl group (**Figure 8, a. & b.**). Additionally, we observed that the morphine group possessed the greatest number of lacunae per mm^3 (M>F>C) but was only significantly different from the control group (**Figure 8, c.**).

Analysis from the final technical report of the same Andronowski Lab rabbit-opioid experiment demonstrated similar pore and lacunae morphometric variable examination of the rabbit femora [103]. The rabbit femora demonstrated greatest % pore volume and pore diameter among the control group (C>M>F), though only significantly different from the fentanyl animals. Additionally, control animals exhibited normal intraskeletal variability among pore and lacunar morphometric variables between femora and tibiae of the same animals. However, opioid exposure resulted in an inversion of these trends [103].

Increased osteocyte lacunar density in the morphine and fentanyl groups was observed. This is an interesting and unanticipated finding because osteocyte lacunar density (# lacunar/mm^3) is often used as representative information regarding cellular presence and remodelling activity during life [21,29]. Osteocyte cells are housed within osteocyte lacunae

throughout life and become more abundant within the bone matrix as a direct result of bone remodelling. Osteocyte lacunar density is influenced by numerous physiological influences and lifestyle factors, including opioid exposure [37]. Greater lacunar density in the morphine group reflects a decoupling of the osteoclasts and osteoblasts in the remodelling process, while also indicating a higher rate of bone turnover which should be associated with new osteocyte lacunae. While osteocyte lacunar density can provide perspective of remodelling activity, there are other factors to consider when conducting a thorough examination of remodelling rate [110–112]. For example, Frost (1960) describes a phenomenon, called micropetrosis, wherein lacunar spaces are unoccupied by osteocytes and are instead filled with minerals (e.g., calcium phosphate)[116]. It is possible that some of the increased lacunar presence may be ascribed to micronecrosis, however, it is not possible to discern what lacunar cells housed living osteocytes and which have undergone micronecrosis using SRμCT.

Statistical analyses indicated that the morphine group demonstrated a greater pore diameter, and greater number of pores compared to the fentanyl group, as well as a greater number of osteocyte lacunae compared to controls. Overall, the morphine group demonstrates the greater cortical porosity between group treatment types. However, this trend is not observed in the fentanyl group. While mechanisms of fentanyl and morphine on bone cell activation are only hypothesized in the literature [7], it is important to recall that experimental drug administration routes were performed differently between fentanyl and morphine (e.g., subcutaneous injection vs. patch) due to recommendations from The University of Akron consulting veterinarian. The use of transdermal patch drug administration posed numerous challenges in the experimental trials that are further discussed in section 4.5 of the discussion. As a result of these issues, we hypothesize that the trends present among morphine animal pore

morphometry are absent in the fentanyl group for these reasons. This is an important consideration as the lack of fentanyl absorption due to application of transdermal patches likely posed a limitation to the interpretation of imaging, biomechanical, and cross-sectional geometric data.

4.2 Cross-Sectional Geometry

We hypothesized that a decrease in cortical area and enlarged medullary cross-sectional area would be present in opioid animals compared to controls. However, visually we can appreciate that opioid animals display greater medullary (F>M>C) and cortical areas (M>F>C) compared to the control group (**Figure 9**). These findings are in-line with our hypotheses and suggest that potentially an increased experimental trial period would allow us to observe further differences in the sample cross-sectional geometry with lengthened treatment periods. The current Andronowski-lab CIHR-funded rabbit opioid experimental model has implemented a longer trial period (from 8 to 12 weeks). Additionally, preliminary work further compared similar cross-sectional geometric properties of the rabbit femora (of the same animal) and found no significant differences between treatment and controls groups [103].

4.3 Biomechanical Findings

Current literature describes a negative relationship between chronic opioid exposure and bone health, bone failure resistance, and the bone remodelling process by interfering with key hormonal regulators of the remodelling process, osteoblast functioning, and bone homeostasis [7,37,38,41–52,54–56]. We hypothesized that opioid exposure would negatively impact bone's resistance to fracture, increase bone failure resistance, and that animals exposed to opioids would

have reduced bone strength. However, when exploring group differences of mean load (N), displacement (mm), test time (s), strength (MPa), and young's modulus (MPa), none of the treatment groups demonstrated significant differences **(Figure 10)**. In alignment with our hypotheses, we observed that the control group appears to have required a greater peak force (N) to induce fracture, and sustained loading for a greater displacement (mm) and duration of time (s) compared to the fentanyl and morphine groups. Additionally, the control group visually, and not statistically significantly, demonstrated the greatest strength (i.e., resistance to failure) and young's modulus (i.e., measure of elasticity) compared to both drug groups.

Current literature further demonstrates that bone microstructure and cross-sectional geometry, among other factors, are characteristics that define bone's behaviour under loading forces [61,73,110]. This study found that there were no significant differences in biomechanical variables between groups despite findings elucidating statistically significant difference among microstructural parameters. The current literature describes that increased porosity is associated with increased bone failure resistance [61,73,110]. Recent work by Jepsen et al (2019) describes a scoring system ("pore score") that quantifies how pore density and distribution impact bending strength[117]. Specifically, pores within closer proximity to the periosteal surface of long bones are more critical-factors in assessing bone bending strength[117]. Additionally, the literature reflects that increased lacunar cell presence are thought to guide crack propagation and initiate tissue failure [118,119]. Despite these findings in the current literature, the morphine group's biomechanical performance did not significantly differ from any other group within this study despite having greater overall porosity.

Additionally, there were no significant differences found between groups among cross-sectional parameters, which are also closely associated with biomechanical performance in the

literature [61]. These considerations suggest that there are likely additional factors that were not examined (e.g,. collagen fibre orientation, osteon circularity, degree of mineralization) that could be explored to bolster our understanding of bone biomechanical performances in the context of both our treatment groups, bone micro- and macro-structural parameters.

The biomechanical tests performed in this study are quasistatic in nature, meaning that load was applied to the sample at slow rate, incrementally [61,113]. It is possible that exploring fatigue testing modalities of biomechanical testing, which employs cyclical loading and unloading of samples to explore a samples material endurance, could provide more data to decipher potential treatment group differences [61,113].

It is also possible that bone samples became dehydrated as a result of opioid exposure, freezing the samples after excision, or ethanol fixation. Despite following specific preservation and rehydration recommendations to best maintain bone biomechanical capabilities (e.g., linear elastic and visco-elastic properties), the samples may have become dehydrated, which can increase sample stiffness, tensile strength, and hardness, thereby obscuring sample trends between groups [74], [76,112,114].

4.4 Correlation analysis

The current literature indicates that pore morphometry greatly influences bone biomechanical performance in a multitude of ways. For example, more circular and smaller osteons can exist more densely in bone which is known to be mechanically advantageous because of the highly mineralized osteon boarders (cement lines) in which deflect microcracks during loading [8,66–69]. Pores are the vascular structures within osteons, and as such, we can

use them as a proxy for osteons. The correlation analysis between pore morphometric variables and biomechanical variables corroborate the literature surrounding this relationship: as demonstrated by the control group, increased pore volume is associated with greater peak force (i.e., the greatest force that the sample can withstand before fracture/failure), in the fentanyl group where increased pore volume is associated with greater flexural modulus (i.e. ability to resist bending), and in the morphine group where increased number of pores per mm^2 are associated with increased flexural modulus. Additionally, we can see specifically that among the fentanyl group, the greater separation between pores is associated with decreased ability to resist bending. These findings corroborate the current literature surrounding the known relationship between pore morphometry and bone biomechanical performance.

Interestingly, we can also see that, among the control group, pore diameter is positively associated with peak force. That is to say that the larger the pores, the greater force required to induce failure in the control samples. This unanticipated finding reflects an inverse relationship to that previously discussed in the literature.

There is a disagreement within the literature concerning the effect of lacunar morphometric variables on bone biomechanical performance. For example, lacunar morphometric variables were positively correlated with flexural modulus and strengths in rats, suggesting that lacunar parameters may be mechanically advantageous [115]. However, lacunae are suggested to guide microcracks throughout tissue and increase lacunar presence has also been associated with regions of initiated tissue failure [103,115–117]. The results of the correlation analysis for this study support the claims within the literature that increased lacunar morphometric parameters are mechanically disadvantageous. For example, increased lacunar connectivity density is associated with decreased bone strength in the control group. Further,

greater lacunar volume, surface, and diameter are correlated with decreased force necessary to initiate fracture (peak force) in the fentanyl group. Conversely, among our results, the morphine group demonstrates that lacunar connectivity density is positively associated with resistance to bending (flexural modulus). This relationship may suggest that increased lacunar connectivity density may create increased rigidity in the morphine bone samples, and thus, despite having increased flexural modulus, does not provide the elasticity necessary to resist failure.

Bone cross-sectional geometry mechanically alters the ways in which a sample behaves under bending forces. A sample with a greater cortical area (cross-sectional area), for example, will demonstrate a greater number of chemical bonds connecting the cross-sectional surfaces [61,70]. Specifically, increased cortical area reflects increased chemical bonds, which suggests increased strength[70]. The distribution of bone tissue also greatly influences bending behaviour, wherein increased distribution of material from the neutral axis will provide more resistance to bending and failure [59,61]. Both the control and the morphine groups demonstrated a positive linear correlation between cortical area and peak force, reinforcing that increased cross-sectional area of a sample will require greater bending forces to initiate fracture. The fentanyl group demonstrated no such trend, however, did demonstrate a negative linear relationship between perimeter and strength. Perimeter, however, does not inform cortical bone tissue presence or distribution.

Correlational analysis demonstrated certain unique findings between pore morphometric variables and cross-sectional geometric parameters. Among the control group, greater pore volume, diameter, and surface are all associated with increased cortical area. Among the fentanyl group, we can appreciate that greater pore surface is associated with greater cortical and medually area. Lastly, among the morphine group, increased pore connectivity density is

associated with greater medullary area. These results suggest that there is a relationship between pore morphometric parameters and cross-sectional geometric properties, but in disorganized ways. Healthy bone remodelling processes will maintain resorption and deposition in equilibrium [1,5,25]. However, the increased medullary area with pore morphometric variables among the fentanyl and morphine groups suggest thinning of the cross-sectional cortical bone cortex. This cortical thinning is not observed in the control group, wherein there is an observable increase in bone cortical tissue at the cross-section associated with increased pore morphometric variables.

Interestingly, the fentanyl group demonstrated significant trends between lacunar morphometric variables and cross-sectional geometric properties that were not present among the control or morphine group. Lacunar morphometric variables such as lacunar volume, diameter, and lacunar surface density demonstrated significant negative correlations with cortical area. Similarly, lacunar volume, diameter, and number of lacunae per mm^3 demonstrated significant negative correlations with medullary area. That is to say that increased lacunar morphometric parameters are associated with less cortical bone and increased medullary space in the fentanyl group. These paired correlations indicate that the cross-section of the fentanyl group samples are shrinking as lacunar parameters increase. These findings suggest that the fentanyl group may be subject to cellular dysregulation because of the drug treatment. The current Andronowski-lab CIHR-funded rabbit opioid experimental model is working to delve into this further.

4.5 Study Limitations

Drug administration

This experimental model employed the use of two different drug administration vehicles: transdermal fentanyl patches (25µg/h slow release) and morphine subcutaneous bolus injections (3mg/kg/day) [89]. The use of transdermal patch drug administration posed numerous challenges

in the experimental trials: rabbit chewing and removal of patches, skin irritation, fur matting, increased grooming behaviour, etc [89]. The variety of drug administration methods poses a limitation to this study as the impacts of this experimental parameter on the results are unknown. Consistent drug administration method would be ideal for continuity within the study and is recommended for future analyses.

Longitudinal blood draws

Longitudinal blood draws were not performed during the experimental period of this study to avoid causing undue stress on the animals [89]. Blood draws would have permitted the evaluation of plasma opioid concentrations throughout the study, and assisted in the confirmation that both drug administration vehicles were delivering their intended dosages [89,118]

Cross-sectional data acquisition

Cross-sectional data for each sample were acquired from the fractured right tibial fragments. A clean cut was made just superior to the fracture borders and subsequently photographed for analysis. This method of cross-sectional data acquisition is limited because it provides cross-sectional information from above the fracture, and not at the fracture location itself.

While this method does provide adequate information about the cross-sectional geometry of each sample, future work should perform μCT imaging experiments on the contralateral limb for each individual before biomechanical testing experiments are conducted. Using sample contralateral limb samples, a) prevents compromising biomechanical testing samples with the heat and dehydrating effects of imaging and b) allows researchers to retain representative cross-

sectional geometric properties about the sample for the approximate fracture location. The use of a contralateral limb for μCT imaging purposes was not possible in this study given that the left rabbit hind-limbs had been used previously for other experiments related to the NIJ research objectives.

Model organism considerations

This is an *ex-vivo* study, and the clinical applications of opioids on bone fracture are an *in-vivo* consideration for the lived experiences of opioid users. It is well documented that remodelling rates can vary between individuals, within a skeleton, between sampling locations on a given skeletal element, and even vary within a cross-section of a singular element [4,14]. It is especially true that we must consider that remodelling rates must vary between species as well. While rabbits remain an excellent model organism for this field of research, it is important to investigate similar research questions within the current clinical literature.

4.6 Public Health Considerations

This project's broader impacts speak to specific demographics at the greatest risk of adverse effects of prolonged opioid use. For example, elderly populations are at the greatest risk as fracture-related falls are the sixth leading cause of death in elderly adults [6,36,37]. Approximately 25% of Canadians aged 40 years and older who experience a hip fracture die within a year of injury [95]. There are unique health care disparities in Newfoundland and Labrador concerning bone fractures: Newfoundland and Labradorians wait on average two days to be seen by a physician after a traumatic bone fracture, and an average of 182 days for hip/knee replacements following injury [96]. This leaves many elderly Newfoundlanders and

Labradorians in pain while awaiting treatment. Clinically, opioids are commonly used for the treatment of moderate to severe pain following traumatic bone fracture [32,50]. Elderly adults are prescribed opioids more than any other age demographic [6,36,37]. In Canada, over 40% of adults ages 55 years and older have used prescription opioids [97,98]. Canadians 65 years and older consistently receive a greater number of opioid prescriptions, and are more likely to be prescribed opioids for pain relief and pursue long-term opioid therapy (24.8%) than any other age group in the country [97,98]. These health disparities are an alarming call to action for research that will focus on improving clinical outcomes and quality of life for older Canadians.

4.7 Future Directions

Andronowski Lab CIHR Rabbit-opioid experiment (2023)

The former Andronowski Lab rabbit-opioid experimental model provided proof-of-principle data that inspired the current Canadian Institute of Health Research (CIHR) rabbit-opioid experimental model that seeks to revise and improve upon previous limitations. In the CIHR-funded project, the Andronowski Lab will conduct a 12-week experimental trial wherein 6 groups of 8 animals each will receive treatment via subcutaneous bolus injections. Each group of 8 animals will consist of 4 males and 4 females to account for sex differences. The group treatment types vary as follows: high fentanyl, low fentanyl, control, high morphine, low morphine, and recovery. The recovery group will receive 8-weeks of opioid treatment followed by 4 weeks of control saline injections. Throughout the experimental trial, longitudinal blood draws will be collected on a weekly basis to assess sex hormones and opioid serum levels. The adjustments made in the CIHR-funded rabbit-opioid experimental model are promising as they

build on the former Andronowski Lab proof-of-principle study in order to eliminate known limitations of the study.

Sex & Gender Considerations

This study's experimental model implements the use of male rabbits as a model organism to examine the impact of opioids on bone failure resistance. However, only using male rabbits in this study limits the interpretation and application of its findings in clinical sectors. Many sex-related considerations related to opioid use, bone health, and bone microstructure (e.g. pain perception, opioid metabolises, menopause, age-related bone degeneration, etc.) exist. While opioids have a well-documented effect on the human endocrine system, impacts of opioids vary between biological sexes [1,21,43,119–121]. Estrogen is a key player in the pain pathway and can influence our individual perceptions of pain [122]. Because females naturally produce more estrogen compared to males, females tend to be more aware of changes in pain severity because of analgesic intervention [122–125]. Consequently, clinical literature reflects that males may require up to 30-40% greater dosage of morphine to acquire the same symptom relief as experienced by their female counterparts[121]. Additionally, estrogen is a key regulator of bone remodelling in females [1,2,11,21,63,126–128]. Postmenopausal females experience a sharp decrease in estrogen, resorption of bone matrix becomes "uncoupled" with new bone deposition, and frequently results in the thinning of the female bone cortex up to 33% [25,129]. Conversely, males experience a steady and slow decline in bone health with some ability to retain cortical area in certain skeletal elements [8,130–136].

While primary biological differences are attributed to sex, however, it is possible that expressions of gender may also have indirect influences. Gender identity can be considered a social determinant of health as well as a key component to an individual's wellness, which can

indirectly impact health outcomes and treatment responses. Sex and gender related differences are critical to consider when exploring the relationship between chronic opioid exposure and bone failure resistance.

In the context of a rabbit experimental model, gender differences are not relevant. However, future studies should explore these sex differences by employing both male and female rabbits to assess the sex-related outcomes of chronic opioid use on bone remodelling and biomechanical performance. Additionally, further research should seek to investigate the health disparities present among marginalized genders and non-gender conforming populations to best appreciate how gender and gender-identity recognition act contributes to the growing list of social determinants of health. An excellent summary of these considerations is provided by Andronowski and Depp (2022), where social and biological risk factors (e.g., age, ancestry, socioeconomic status, housing instability, education, etc) of opioid abuse are discussed in detail [137].

Stress Considerations

Stress is an important consideration when evaluating bone health in both human and animal populations. The effects of the stress hormone cortisol on bone health are well-documented in the current literature. Cortisol is known to dysregulate the bone formation processes and decrease bone mineral density [136]. Further, high levels of cortisol throughout ageing stimulate BMU apoptosis and suppress new osteoblast formation, thus indirectly increasing bone failure resistance [136,138,139]. Additionally, BMUs possess noradrenaline and neuropeptides receptors, making BMUs directly impacted by physiological stress [140,141].

Despite best efforts, it is possible that the rabbit opioid-experimental model may have subjected rabbits to varying degrees of stress throughout the experimental period (e.g. as a result of daily injections, irritations, handling, laboratory environment, etc.). Consideration for these stress levels should eb considered when interpreting data. Future work should consider longitudinal blood draws to measure cortisol levels and investigate the potential adverse effects of the stress hormone on the bone remodelling process and bone biomechanical performance.

Tissue Material & Architectural Considerations

Bone biomechanical performance is subject to numerous influences. While examining bone microstructure, cross-sectional geometry, and descriptors of bone biomechanical performance is a thorough examination of these factors, it is also important to consider the tissue material and architectural properties of bone. For example, both collagen fiber orientation and bone mineral density are well-studied factors that influence structural competency and bone failure resistance in bone samples [23,61,64,103,142]. Future work should consider exploring both bone mineral density and collagen fiber orientation to best formulate a comprehensive analysis surrounding the exploration of the effect of opioid use on the biomechanical parameters of bone.

5. Conclusion

This study examined the microstructural, cross-sectional geometric, and biomechanical parameters of rabbit tibiae among three treatment experimental groups (control, morphine, fentanyl). A multi-modal approach was used to collect data including methods of bone microstructure visualisation (via SRμCT imaging experiments), extraction of cross-sectional geometric properties (BoneJ), and biomechanical testing (3-point bend testing) to assess structural competence and bone failure resistance. Numerous factors exist that influence a bone's biomechanical performance under loading forces. Combining biomechanical testing data, SRμCT imaging experiments, and cross-sectional geometric properties of the bone samples allowed us to characterize the material properties of bone in this novel animal model system. By exploring the relationship of these factors, we can help elucidate the working predictive methods for anticipating structural competence and bone failure resistance among opioid and control animals. Analyses revealed significantly greater cortical porosity in the morphine group compared to the other treatment types. Qualitatively, we observed differences between treatment groups such as greater medullary and cortical areas in the fentanyl groups, and greater markers of structural competence (peak force, young's modulus, strength, displacement) among the control group.

Correlational analyses of SRμCT, cross-sectional geometric, and 3-point bend test data allowed for the associated of structure with function to analyze the expected indirect effects of opioid use on bone biomechanical parameters. The trends from the correlation analysis demonstrate that pores can be used as a proxy for osteons, and that smaller and more densely packed osteons are mechanically advantageous across all treatment types. Conversely, lacunar morphometric variables within this study demonstrate reduced structural competency.

Additionally, increased cortical area and medullary area are mechanically advantageous so long as the increased medullary area does not create thinning of the bone cortex. Ultimately, the relationship between pore and lacunar morphometric data with cross-sectional geometry suggests thinning of the bone cortex and cellular dysregulation of the remodelling process in the opioid experimental groups.

The proposed work is culturally relevant as the misuse and addiction to prescription opioids (and illicit synthetic opioids) continues to be a serious public health crisis nationwide. It offers insight relating to the possible clinical effects of prolonged opioid use in humans. Further, this project's larger application speaks to specific demographics at the largest risk of adverse effects of prolonged opioid use (e.g., elderly populations, recreational opioid users, patients using opioids for pain management, etc.). The research presented here is a necessary step towards 1) identifying preventative measures and suitable time frames for pharmaceutical treatments, and 2) follow-up interventions targeted to bone health for recovering opioid users at increased risk of bone fracture.

References

1. Walsh, J.S. Normal Bone Physiology, Remodelling and Its Hormonal Regulation. *Surg. Oxf.* **2015**, *33*, 1–6, doi:10.1016/j.mpsur.2014.10.010.

2. Buikstra, J.E. *Ortner's Identification of Pathological Conditions in Human Skeletal Remains*; 2019; ISBN 978-0-12-809738-0.

3. White, T.D.; Folkens, P.A. *The Human Bone Manual*; Elsevier Academic: Amsterdam ; Boston, 2005; ISBN 978-0-12-088467-4.

4. Frost, H.M. Tetracyline-Based Histological Analysis of Bone Remodeling. *Calcified Tissue Research* **1969**, 211=237.

5. Allen, M.R.; Burr, D.B. Chapter 4 - Bone Modeling and Remodeling. In *Basic and Applied Bone Biology*; Burr, D.B., Allen, M.R., Eds.; Academic Press: San Diego, 2014; pp. 75–90 ISBN 978-0-12-416015-6.

6. Verborgt, O.; Tatton, N.A.; Majeska, R.J.; Schaffler, M.B. Spatial Distribution of Bax and Bcl-2 in Osteocytes after Bone Fatigue: Complementary Roles in Bone Remodeling Regulation. *J. Bone Miner. Res.* **2002**, *17*, 907–914, doi:10.1359/jbmr.2002.17.5.907.

7. Coluzzi, F.; Mattia, C.; Raffa, R.R.; Pergolizzi, J. The Unsolved Case of "Bone-Impairing Analgesics": The Endocrine Effects of Opioids on Bone Metabolism. *Ther. Clin. Risk Manag.* **2015**, 515, doi:10.2147/TCRM.S79409.

8. Andronowski, J.M.; Cole, M.E. Current and Emerging Histomorphometric and Imaging Techniques for Assessing Age□at□death and Cortical Bone Quality. *WIREs Forensic Sci.* **2021**, *3*, doi:10.1002/wfs2.1399.

9. Parfitt, A.M. The Cellular Basis of Bone Remodeling: The Quantum Concept Reexamined in Light of Recent Advances in the Cell Biology of Bone. *Calcif. Tissue Int.* **1984**,

36, S37–S45, doi:10.1007/BF02406132.

10. Frost, H.M. Bone "Mass" and the "Mechanostat": A Proposal. *Anat. Rec.* **1987**, *219*, 1–9, doi:10.1002/ar.1092190104.

11. Robling, A.G.; Castillo, A.B.; Turner, C.H. Biomechanical and Molecular Regulation of Bone Remodeling. *Annu. Rev. Biomed. Eng.* **2006**, *8*, 455–498, doi:10.1146/annurev.bioeng.8.061505.095721.

12. Martin, R.B. On the Significance of Remodeling Space and Activation Rate Changes in Bone Remodeling. *Bone* **1991**, *12*, 391–400, doi:10.1016/8756-3282(91)90028-H.

13. Pfeiffer, S.; Lazenby, R.; Chiang, J. Cortical Remodeling Data Are Affected by Sampling Location. *Am. J. Phys. Anthropol.* **1995**, *96*, 89–92, doi:10.1002/ajpa.1330960110.

14. Maggiano, C.M. A Microstructural Perspective on Bone Modeling during Growth and Mechanical Adaptation. **2012**.

15. Tomes, J.; Morgan, C. IV. Observations on the Structure and Development of Bone. *Philos. Trans. R. Soc. Lond.* **1853**, *143*, 109–139, doi:10.1098/rstl.1853.0004.

16. Johnson, L.C. *(1964). Morphologic Analysis of Pathology. In H. M. Frost (Ed.), Bone Biodynamics (Pp. 543–654).*; Little, Brown & Co.: Bonston, MA, 1964;

17. Hattner, R.; Epker, B.N.; Frost, H.M. Suggested Sequential Mode of Control of Changes in Cell Behaviour in Adult Bone Remodelling. *Nature* **1965**, *206*, 489–490, doi:10.1038/206489a0.

18. Martin, R.B.; Burr, D.B.; Sharkey, N.A.; Fyhrie, D.P. *Skeletal Tissue Mechanics*; Springer New York: New York, NY, 2015; ISBN 978-1-4939-3001-2.

19. Harrison, K.D.; Hiebert, B.D.; Panahifar, A.; Andronowski, J.M.; Ashique, A.M.; King, G.A.; Arnason, T.; Swekla, K.J.; Pivonka, P.; Cooper, D.M. Cortical Bone Porosity in Rabbit

Models of Osteoporosis. *J. Bone Miner. Res.* **2020**, *35*, 2211–2228, doi:10.1002/jbmr.4124.

20. Hall, B.K. *Bones and Cartilage: Developmental and Evolutionary Skeletal Biology*; Second edition.; Elsevier/AP, Academic Press is an imprint of Elsevier: Amsterdam, 2015; ISBN 978-0-12-416678-3.

21. Robling, A.G.; Turner, C.H. Mechanical Signaling for Bone Modeling and Remodeling. *Crit. Rev. Eukaryot. Gene Expr.* **2009**, *19*, 319–338, doi:10.1615/CritRevEukarGeneExpr.v19.i4.50.

22. Frost, H.M. Bone Microdamage: Factors That Impair Its Repair. *Curr. Concepts Bone Fragility Springer Berl. Heidelb.* **1986**, 123–148.

23. Lee, T.C.; Staines, A.; Taylor, D. Bone Adaptation to Load: Microdamage as a Stimulus for Bone Remodelling. *J. Anat.* **2002**, *201*, 437–446, doi:10.1046/j.1469-7580.2002.00123.x.

24. Parfitt, A.M. Bone Histomorphometry: Proposed System for Standardization of Nomenclature, Symbols, and Units. *Calcif. Tissue Int.* **1988**, *42*, 284–286, doi:10.1007/BF02556360.

25. Parfitt, A.M. The Coupling of Bone Formation to Bone Resorption: A Critical Analysis of the Concept and of Its Relevance to the Pathogenesis of Osteoporosis. *Metab. Bone Dis. Relat. Res.* **1982**, *4*, 1–6, doi:10.1016/0221-8747(82)90002-9.

26. Andreasen, C.M.; Ding, M.; Overgaard, S.; Bollen, P.; Andersen, T.L. A Reversal Phase Arrest Uncoupling the Bone Formation and Resorption Contributes to the Bone Loss in Glucocorticoid Treated Ovariectomised Aged Sheep. *Bone* **2015**, *75*, 32–39, doi:10.1016/j.bone.2015.02.014.

27. Hinge, M.; Delaisse, J.-M.; Plesner, T.; Clasen-Linde, E.; Salomo, M.; Andersen, T.L. High-Dose Therapy Improves the Bone Remodelling Compartment Canopy Coverage and Bone

Formation in Multiple Myeloma. *Br. J. Haematol.* **2015**, *171*, 355–365, doi:10.1111/bjh.13584.

28. Jensen, P.R.; Andersen, T.L.; Hauge, E.-M.; Bollerslev, J.; Delaissé, J.-M. A Joined Role of Canopy and Reversal Cells in Bone Remodeling — Lessons from Glucocorticoid-Induced Osteoporosis. *Bone* **2015**, *73*, 16–23, doi:10.1016/j.bone.2014.12.004.

29. Himeno-Ando, A.; Izumi, Y.; Yamaguchi, A.; Iimura, T. Structural Differences in the Osteocyte Network between the Calvaria and Long Bone Revealed by Three-Dimensional Fluorescence Morphometry, Possibly Reflecting Distinct Mechano-Adaptations and Sensitivities. *Biochem. Biophys. Res. Commun.* **2012**, *417*, 765–770, doi:10.1016/j.bbrc.2011.12.031.

30. Basso, N.; Heersche, J.N.M. Effects of Hind Limb Unloading and Reloading on Nitric Oxide Synthase Expression and Apoptosis of Osteocytes and Chondrocytes. *Bone* **2006**, *39*, 807–814, doi:10.1016/j.bone.2006.04.014.

31. Aguirre, J.I.; Plotkin, L.I.; Stewart, S.A.; Weinstein, R.S.; Parfitt, A.M.; Manolagas, S.C.; Bellido, T. Osteocyte Apoptosis Is Induced by Weightlessness in Mice and Precedes Osteoclast Recruitment and Bone Loss. *J. Bone Miner. Res.* **2006**, *21*, 605–615, doi:10.1359/jbmr.060107.

32. Gross, T.S.; Akeno, N.; Clemens, T.L.; Komarova, S.; Srinivasan, S.; Weimer, D.A.; Mayorov, S. Selected Contribution: Osteocytes Upregulate HIF-1α in Response to Acute Disuse and Oxygen Deprivation. *J. Appl. Physiol.* **2001**, *90*, 2514–2519, doi:10.1152/jappl.2001.90.6.2514.

33. Gross, T.S.; King, K.A.; Rabaia, N.A.; Pathare, P.; Srinivasan, S. Upregulation of Osteopontin by Osteocytes Deprived of Mechanical Loading or Oxygen. *J. Bone Miner. Res.* **2004**, *20*, 250–256, doi:10.1359/JBMR.041004.

34. Noble, B.S.; Peet, N.; Stevens, H.Y.; Brabbs, A.; Mosley, J.R.; Reilly, G.C.; Reeve, J.;

Skerry, T.M.; Lanyon, L.E. Mechanical Loading: Biphasic Osteocyte Survival and Targeting of Osteoclasts for Bone Destruction in Rat Cortical Bone. *Am. J. Physiol.-Cell Physiol.* **2003**, *284*, C934–C943, doi:10.1152/ajpcell.00234.2002.

35. Verborgt, O.; Gibson, G.J.; Schaffler, M.B. Loss of Osteocyte Integrity in Association with Microdamage and Bone Remodeling after Fatigue in Vivo. *J. Bone Miner. Res.* **2000**, *15*, 60–67, doi:10.1359/jbmr.2000.15.1.60.

36. Robling, A.G.; Duijvelaar, K.M.; Geevers, J.V.; Ohashi, N.; Turner, C.H. Modulation of Appositional and Longitudinal Bone Growth in the Rat Ulna by Applied Static and Dynamic Force. *Bone* **2001**, *29*, 105–113, doi:10.1016/S8756-3282(01)00488-4.

37. Mohamad, N.V.; Soelaiman, I.-N.; Chin, K.-Y. A Concise Review of Testosterone and Bone Health. *Clin. Interv. Aging* **2016**, *Volume 11*, 1317–1324, doi:10.2147/CIA.S115472.

38. Boshra, V. Evaluation of Osteoporosis Risk Associated with Chronic Use of Morphine, Fentanyl and Tramadol in Adult Female Rats. *Curr. Drug Saf.* **2011**, *6*, 159–163, doi:10.2174/157488611797579267.

39. Baldini, A.; Von Korff, M.; Lin, E.H.B. A Review of Potential Adverse Effects of Long-Term Opioid Therapy: A Practitioner's Guide. *Prim. Care Companion CNS Disord.* **2012**, doi:10.4088/PCC.11m01326.

40. King, T.; Vardanyan, A.; Majuta, L.; Melemedjian, O.; Nagle, R.; Cress, A.E.; Vanderah, T.W.; Lai, J.; Porreca, F. Morphine Treatment Accelerates Sarcoma-Induced Bone Pain, Bone Loss, and Spontaneous Fracture in a Murine Model of Bone Cancer. *Pain* **2007**, *132*, 154–168, doi:10.1016/j.pain.2007.06.026.

41. Benyamin, R. Opioid Complications and Side Effects. *Pain Physician* **2008**, *2s;11*, S105–S120, doi:10.36076/ppj.2008/11/S105.

42. Jain, N.; Himed, K.; Toth, J.M.; Briley, K.C.; Phillips, F.M.; Khan, S.N. Opioids Delay Healing of Spinal Fusion: A Rabbit Posterolateral Lumbar Fusion Model. *Spine J.* **2018**, *18*, 1659–1668, doi:10.1016/j.spinee.2018.04.012.

43. Brennan, M.J. The Effect of Opioid Therapy on Endocrine Function. *Am. J. Med.* **2013**, *126*, S12–S18, doi:10.1016/j.amjmed.2012.12.001.

44. Rubenstein, L.Z.; Josephson, K.R. Falls and Their Prevention in Elderly People: What Does the Evidence Show? *Med. Clin. North Am.* **2006**, *90*, 807–824, doi:10.1016/j.mcna.2006.05.013.

45. Buckeridge, D.; Huang, A.; Hanley, J.; Kelome, A.; Reidel, K.; Verma, A.; Winslade, N.; Tamblyn, R. Risk of Injury Associated with Opioid Use in Older Adults: Injury Related to Opioid Use. *J. Am. Geriatr. Soc.* **2010**, *58*, 1664–1670, doi:10.1111/j.1532-5415.2010.03015.x.

46. Rosen, H.; Bar-Shavit, Z. Dual Role of Osteoblastic Proenkephalin Derived Peptides in Skeletal Tissues. *J. Cell. Biochem.* **1994**, *55*, 334–339, doi:10.1002/jcb.240550310.

47. Pérez-Castrillón, J.L.; Olmos, J.M.; Gómez, J.J.; Barrallo, A.; Riancho, J.A.; Perera, L.; Valero, C.; Amado, J.A.; González-Macías, J. Expression of Opioid Receptors in Osteoblast-like MG-63 Cells, and Effects of Different Opioid Agonists on Alkaline Phosphatase and Osteocalcin Secretion by These Cells. *Neuroendocrinology* **2000**, *72*, 187–194, doi:10.1159/000054586.

48. Rico, H.; Costales, C.; Cabranes, J.A.; Escudero, M. Lower Serum Osteocalcin Levels in Pregnant Drug Users and Their Newborns at the Time of Delivery. *Obstet. Gynecol.* **1990**, *75*, 998–1000.

49. Daniell, H.W.; Lentz, R.; Mazer, N.A. Open-Label Pilot Study of Testosterone Patch Therapy in Men with Opioid-Induced Androgen Deficiency. *J. Pain* **2006**, *7*, 200–210, doi:10.1016/j.jpain.2005.10.009.

50. Daniell, H.W. Hypogonadism in Men Consuming Sustained-Action Oral Opioids. *J. Pain* **2002**, *3*, 377–384, doi:10.1054/jpai.2002.126790.

51. Daniell, H.W. DHEAS Deficiency during Consumption of Sustained-Action Prescribed Opioids: Evidence for Opioid-Induced Inhibition of Adrenal Androgen Production. *J. Pain* **2006**, *7*, 901–907, doi:10.1016/j.jpain.2006.04.011.

52. Facchinetti, F.; Comitini, G.; Petraglia, F.; Volpe, A.; Genazzani, A.R. Reduced Estriol and Dehydroepiandrosterone Sulphate Plasma Levels in Methadone-Addicted Pregnant Women. *Eur. J. Obstet. Gynecol. Reprod. Biol.* **1986**, *23*, 67–73, doi:10.1016/0028-2243(86)90106-1.

53. Rajagopal, A.; Vassilopoulou-Sellin, R.; Palmer, J.L.; Kaur, G.; Bruera, E. Hypogonadism and Sexual Dysfunction in Male Cancer Survivors Receiving Chronic Opioid Therapy. *J. Pain Symptom Manage.* **2003**, *26*, 1055–1061, doi:10.1016/s0885-3924(03)00331-2.

54. Bliesener, N.; Albrecht, S.; Schwager, A.; Weckbecker, K.; Lichtermann, D.; Klingmüller, D. Plasma Testosterone and Sexual Function in Men Receiving Buprenorphine Maintenance for Opioid Dependence. *J. Clin. Endocrinol. Metab.* **2005**, *90*, 203–206, doi:10.1210/jc.2004-0929.

55. Oltmanns, K.M.; Fehm, H.L.; Peters, A. Chronic Fentanyl Application Induces Adrenocortical Insufficiency. *J. Intern. Med.* **2005**, *257*, 478–480, doi:10.1111/j.1365-2796.2005.01483.x.

56. Hall, G.M.; Lacoumenta, S.; Hart, G.R.; Burrin, J.M. Site of Action of Fentanyl in Inhibiting the Pituitary-Adrenal Response to Surgery in Man. *Br. J. Anaesth.* **1990**, *65*, 251–253, doi:10.1093/bja/65.2.251.

57. Ottawa: Public Health Agency of Canada Special Advisory Committee on the Epidemic of Opioid Overdoses. National Report: Apparent Opioid-Related Deaths in Canada (January

2016 to September 2017) Web-Based Report. 2018.

58. Federal, provincial, and territorial Special Advisory Committee on the Epidemic of Opioid Overdoses. *Opioid- and Stimulant-Related Harms in Canada. Ottawa: Public Health Agency of Canada.*; 2023;

59. Larsen, C.S. *Bioarchaeology: Interpreting Behavior from the Human Skeleton*; 2nd ed.; Cambridge University Press, 2015; ISBN 978-0-521-83869-6.

60. Roylance, D. Introduction to Elasticity. **2000**.

61. Cole, J.H.; van der Meulen, M.C.H. Biomechanics of Bone. In *Osteoporosis*; Adler, R.A., Ed.; Humana Press: Totowa, NJ, 2010; pp. 157–179 ISBN 978-1-934115-19-0.

62. Sims, N.A.; Martin, T.J. Coupling the Activities of Bone Formation and Resorption: A Multitude of Signals within the Basic Multicellular Unit. *BoneKEy Rep.* **2014**, *3*, doi:10.1038/bonekey.2013.215.

63. Almeida, M.; Laurent, M.R.; Dubois, V.; Claessens, F.; O'Brien, C.A.; Bouillon, R.; Vanderschueren, D.; Manolagas, S.C. Estrogens and Androgens in Skeletal Physiology and Pathophysiology. *Physiol. Rev.* **2017**, *97*, 135–187, doi:10.1152/physrev.00033.2015.

64. Mirzaali, M.J.; Libonati, F.; Ferrario, D.; Rinaudo, L.; Messina, C.; Ulivieri, F.M.; Cesana, B.M.; Strano, M.; Vergani, L. Determinants of Bone Damage: An Ex-Vivo Study on Porcine Vertebrae. *PLOS ONE* **2018**, *13*, e0202210, doi:10.1371/journal.pone.0202210.

65. Smith, R.W.; Walker, R.R. Femoral Expansion in Aging Women: Implications for Osteoporosis and Fractures. *Science* **1964**, *145*, 156–157, doi:10.1126/science.145.3628.156.

66. Dominguez, V.M.; Agnew, A.M. Microdamage as a Bone Quality Component: Practical Guidelines for the Two□dimensional Analysis of Linear Microcracks in Human Cortical Bone. *JBMR Plus* **2019**, *3*, e10203, doi:10.1002/jbm4.10203.

67. Van Oers, R.F.M.; Ruimerman, R.; Van Rietbergen, B.; Hilbers, P.A.J.; Huiskes, R. Relating Osteon Diameter to Strain. *Bone* **2008**, *43*, 476–482, doi:10.1016/j.bone.2008.05.015.

68. Norman, T.L.; Wang, Z. Microdamage of Human Cortical Bone: Incidence and Morphology in Long Bones. *Bone* **1997**, *20*, 375–379, doi:10.1016/S8756-3282(97)00004-5.

69. Yeni, Y.N.; Brown, C.U.; Wang, Z.; Norman, T.L. The Influence of Bone Morphology on Fracture Toughness of the Human Femur and Tibia. *Bone* **1997**, *21*, 453–459, doi:10.1016/S8756-3282(97)00173-7.

70. Roylance, D. INTRODUCTION TO ELASTICITY. **2000**.

71. Akkus, O.; Korkusuz, F.; Akin, S.; Akkas, N. Relation between Mechanical Stiffness and Vibration Transmission of Fracture Callus: An Experimental Study on Rabbit Tibia. *Proc. Inst. Mech. Eng. [H]* **1998**, *212*, 327–336, doi:10.1243/0954411981534105.

72. Currey, J.D. The Effect of Porosity and Mineral Content on the Young's Modulus of Elasticity of Compact Bone. *J. Biomech.* **1988**, *21*, 131–139, doi:10.1016/0021-9290(88)90006-1

73. Schneider, P.; Voide, R.; Stampanoni, M.; Donahue, L.R.; Müller, R. The Importance of the Intracortical Canal Network for Murine Bone Mechanics. *Bone* **2013**, *53*, 120–128, doi:10.1016/j.bone.2012.11.024.

74. Nazarian, A.; Hermannsson, B.J.; Muller, J.; Zurakowski, D.; Snyder, B.D. Effects of Tissue Preservation on Murine Bone Mechanical Properties. *J. Biomech.* **2009**, *42*, 82–86, doi:10.1016/j.jbiomech.2008.09.037.

75. Broz, J.J.; Simske, S.J.; Greenberg, A.R.; Luttges, M.W. Effects of Rehydration State on the Flexural Properties of Whole Mouse Long Bones. **1993**.

76. Sedlin, E.D.; Hirsch, C. Factors Affecting the Determination of the Physical Properties of Femoral Cortical Bone. *Acta Orthop. Scand.* **1966**, *37*, 29–48, doi:10.3109/17453676608989401.

77. Currey, J.D.; Brear, K.; Zioupos, P.; Reilly, G.C. Effect of Formaldehyde Fixation on Some Mechanical Properties of Bovine Bone. *Biomaterials* **1995**, *16*, 1267–1271, doi:10.1016/0142-9612(95)98135-2.

78. Broz, J.J.; Simske, S.J.; Greenberg, A.R.; Luttges, M.W. Effects of Rehydration State on the Flexural Properties of Whole Mouse Long Bones. *J. Biomech. Eng.* **1993**, *115*, 447–449, doi:10.1115/1.2895510.

79. Jee, W.S.; Yao, W. Overview: Animal Models of Osteopenia and Osteoporosis. *J. Musculoskelet. Neuronal Interact.* **2001**, *1*, 193–207.

80. Reinwald, S.; Burr, D. Review of Nonprimate, Large Animal Models for Osteoporosis Research. *J. Bone Miner. Res.* **2008**, *23*, 1353–1368, doi:10.1359/jbmr.080516.

81. Sietsema, W.K. Animal Models of Cortical Porosity. *Bone* **1995**, *17*, S297–S305, doi:10.1016/8756-3282(95)00307-Y.

82. Thompson, D.D.; Simmons, H.A.; Pirie, C.M.; Ke, H.Z. FDA Guidelines and Animal Models for Osteoporosis. *Bone* **1995**, *17*, S125–S133, doi:10.1016/8756-3282(95)00285-L.

83. Recker, R.R.; Kimmel, D.B.; Dempster, D.; Weinstein, R.S.; Wronski, T.J.; Burr, D.B. Issues in Modern Bone Histomorphometry. *Bone* **2011**, *49*, 955–964, doi:10.1016/j.bone.2011.07.017.

84. Pazzaglia, U.E.; Congiu, T.; Raspanti, M.; Ranchetti, F.; Quacci, D. Anatomy of the Intracortical Canal System: Scanning Electron Microscopy Study in Rabbit Femur. *Clin. Orthop.* **2009**, *467*, 2446–2456, doi:10.1007/s11999-009-0806-x.

85. Pazzaglia, U.E.; Bonaspetti, G.; Rodella, L.F.; Ranchetti, F.; Azzola, F. Design, Morphometry and Development of the Secondary Osteonal System in the Femoral Shaft of the Rabbit. *J. Anat.* **2007**, *211*, 303–312, doi:10.1111/j.1469-7580.2007.00782.x.

86. Pazzaglia, U.E.; Zarattini, G.; Giacomini, D.; Rodella, L.; Menti, A.M.; Feltrin, G. Morphometric Analysis of the Canal System of Cortical Bone: An Experimental Study in the Rabbit Femur Carried out with Standard Histology and Micro-CT. *Anat. Histol. Embryol.* **2010**, *39*, 17–26, doi:10.1111/j.1439-0264.2009.00973.x.

87. Gilsanz, V.; Roe, T.F.; Gibbens, D.T.; Schulz, E.E.; Carlson, M.E.; Gonzalez, O.; Boechat, M.I. Effect of Sex Steroids on Peak Bone Density of Growing Rabbits. *Am. J. Physiol.-Endocrinol. Metab.* **1988**, *255*, E416–E421, doi:10.1152/ajpendo.1988.255.4.E416.

88. Newman, E. The Potential of Sheep for the Study of Osteopenia: Current Status and Comparison with Other Animal Models. *Bone* **1995**, *16*, 277S-284S, doi:10.1016/8756-3282(95)00026-A.

89. Andronowski, J.M.; Schuller, A.J.; Cole, M.E.; LaMarca, A.R.; Davis, R.A.; Tubo, G.R. Rabbits (Oryctolagus Cuniculus) as a Model System for Longitudinal Experimental Opioid Treatments: Implications for Orthopedic and Biomedical Research. *Osteology* **2021**, *1*, 225–237, doi:10.3390/osteology1040021.

90. Izakovicova, P.; Borens, O.; Trampuz, A. Periprosthetic Joint Infection: Current Concepts and Outlook. *EFORT Open Rev.* **2019**, *4*, 482–494, doi:10.1302/2058-5241.4.180092.

91. Chae, K.; Jang, W.Y.; Park, K.; Lee, J.; Kim, H.; Lee, K.; Lee, C.K.; Lee, Y.; Lee, S.H.; Seo, J. Antibacterial Infection and Immune-Evasive Coating for Orthopedic Implants. *Sci. Adv.* **2020**, *6*, eabb0025, doi:10.1126/sciadv.abb0025.

92. Bottagisio, M.; Coman, C.; Lovati, A.B. Animal Models of Orthopaedic Infections. A Review of Rabbit Models Used to Induce Long Bone Bacterial Infections. *J. Med. Microbiol.* **2019**, *68*, 506–537, doi:10.1099/jmm.0.000952.

93. Dai, Y.; Lu, J.; Li, F.; Yang, G.; Ji, G.; Wang, F. Changes in Cartilage and Subchondral

Bone in a Growing Rabbit Experimental Model of Developmental Trochlear Dysplasia of the Knee. *Connect. Tissue Res.* **2021**, *62*, 299–312, doi:10.1080/03008207.2019.1697245.

94. Grover, D.M.; Chen, A.A.; Hazelwood, S.J. Biomechanics of the Rabbit Knee and Ankle: Muscle, Ligament, and Joint Contact Force Predictions. *J. Biomech.* **2007**, *40*, 2816–2821, doi:10.1016/j.jbiomech.2007.01.002.

95. Gushue, D.L.; Houck, J.; Lerner, A.L. Rabbit Knee Joint Biomechanics: Motion Analysis and Modeling of Forces during Hopping. *J. Orthop. Res.* **2005**, *23*, 735–742, doi:10.1016/j.orthres.2005.01.005.

96. University of Saskatchewan What Is a Synchrotron? Available online: https://my.matterport.com/show/?m=zCc11EmLM3K (accessed on 18 April 2023).

97. Andronowski, J.M.; Crowder, C.; Soto Martinez, M. Recent Advancements in the Analysis of Bone Microstructure: New Dimensions in Forensic Anthropology. *Forensic Sci. Res.* **2018**, *3*, 294–309, doi:10.1080/20961790.2018.1483294.

98. Cooper BML; Thomas CDL; Clement JG *Technological Developments in the Analysis of Cortical Bone Histology: The Third Dimension and Its Potential in Anthropology. In: Crowder C, Stout SD, Editors. Bone Histology: An Anthropological Perspective.*; CRC Press: Boca Ranton (FL), 2012;

99. Carter, Y.; Thomas, C.D.L.; Clement, J.G.; Peele, A.G.; Hannah, K.; Cooper, D.M.L. Variation in Osteocyte Lacunar Morphology and Density in the Human Femur--a Synchrotron Radiation Micro-CT Study. *Bone* **2013**, *52*, 126–132, doi:10.1016/j.bone.2012.09.010.

100. Carter, Y.; Thomas, C.D.L.; Clement, J.G.; Cooper, D.M.L. Femoral Osteocyte Lacunar Density, Volume and Morphology in Women across the Lifespan. *J. Struct. Biol.* **2013**, *183*, 519–526, doi:10.1016/j.jsb.2013.07.004.

101. Carter, Y.; Suchorab, J.L.; Thomas, C.D.L.; Clement, J.G.; Cooper, D.M.L. Normal Variation in Cortical Osteocyte Lacunar Parameters in Healthy Young Males. *J. Anat.* **2014**, *225*, 328–336, doi:10.1111/joa.12213.

102. Andronowski, J.M.; Davis, R.A.; Holyoke, C.W. A Sectioning, Coring, and Image Processing Guide for High-Throughput Cortical Bone Sample Procurement and Analysis for Synchrotron Micro-CT. *J. Vis. Exp.* **2020**, 61081, doi:10.3791/61081.

103. Andronowski, J.M. *Logitudinal Effects of Prolonged Opioid Use on Cortical Bone Remodelling in a Rabbit Model: Final Technical Report.*; The University of Akron: 302 Buchtel Common Akron, OH, 44325-9001, 2021;

104. Dragonfly 2022.2 [Computer Software]. Object Research Systems (ORS) Inc, Montreal, Canada, 2022; Software Available at Http://Www.Theobjects.Com/Dragonfly.

105. Schneider, C.A.; Rasband, W.S.; Eliceiri, K.W. NIH Image to ImageJ: 25 Years of Image Analysis. *Nat. Methods* **2012**, *9*, 671–675, doi:10.1038/nmeth.2089.

106. Doube, M.; Kłosowski, M.M.; Arganda-Carreras, I.; Cordelières, F.P.; Dougherty, R.P.; Jackson, J.S.; Schmid, B.; Hutchinson, J.R.; Shefelbine, S.J. BoneJ: Free and Extensible Bone Image Analysis in ImageJ. *Bone* **2010**, *47*, 1076–1079, doi:10.1016/j.bone.2010.08.023.

107. Hart, N.H.; Nimphius, S.; Rantalainen, T.; Ireland, A.; Siafarikas, A.; Newton, R.U. Mechanical Basis of Bone Strength: Influence of Bone Material, Bone Structure and Muscle Action. *J. Musculoskelet. Neuronal Interact.* **2017**, *17*, 114–139.

108. Bouxsein, M.L.; Karasik, D. Bone Geometry and Skeletal Fragility. *Curr. Osteoporos. Rep.* **2006**, *4*, 49–56, doi:10.1007/s11914-006-0002-9.

109. Martin, R.M.; Correa, P.H.S. Bone Quality and Osteoporosis Therapy. *Arq. Bras. Endocrinol. Metabol.* **2010**, *54*, 186–199, doi:10.1590/S0004-27302010000200015.

110. Tiede-Lewis, L.M.; Dallas, S.L. Changes in the Osteocyte Lacunocanalicular Network with Aging. *Bone* **2019**, *122*, 101–113, doi:10.1016/j.bone.2019.01.025.

111. Busse, B.; Djonic, D.; Milovanovic, P.; Hahn, M.; Püschel, K.; Ritchie, R.O.; Djuric, M.; Amling, M. Decrease in the Osteocyte Lacunar Density Accompanied by Hypermineralized Lacunar Occlusion Reveals Failure and Delay of Remodeling in Aged Human Bone: Osteocyte Lacunar Density and Composition in Aging. *Aging Cell* **2010**, *9*, 1065–1075, doi:10.1111/j.1474-9726.2010.00633.x.

112. Smith, J.W.; Walmsley, R. Factors Affecting the Elasticity of Bone. *J. Anat.* **1959**, *93*, 503–523.

113. Budynas, R.G.; Roark, R.J.; Sadegh, A.M. *"Beams: Flexure of Straight Bars." Chap. 8. in Roark's Formulas for Stress and Strain.*; Ninth edition.; McGraw-Hill: New York Chicago San Francisco, 2020; ISBN 978-1-260-45375-1.

114. Nyman, J.S.; Roy, A.; Shen, X.; Acuna, R.L.; Tyler, J.H.; Wang, X. The Influence of Water Removal on the Strength and Toughness of Cortical Bone. *J. Biomech.* **2006**, *39*, 931–938, doi:10.1016/j.jbiomech.2005.01.012.

115. Sang, W.; Li, Y.; Guignon, J.; Liu, X.S.; Ural, A. Structural Role of Osteocyte Lacunae on Mechanical Properties of Bone Matrix: A Cohesive Finite Element Study. *J. Mech. Behav. Biomed. Mater.* **2022**, *125*, 104943, doi:10.1016/j.jmbbm.2021.104943.

116. Voide, R.; Schneider, P.; Stauber, M.; Wyss, P.; Stampanoni, M.; Sennhauser, U.; van Lenthe, G.H.; Müller, R. Time-Lapsed Assessment of Microcrack Initiation and Propagation in Murine Cortical Bone at Submicrometer Resolution. *Bone* **2009**, *45*, 164–173, doi:10.1016/j.bone.2009.04.248.

117. Giner, E.; Arango, C.; Vercher, A.; Javier Fuenmayor, F. Numerical Modelling of the

Mechanical Behaviour of an Osteon with Microcracks. *J. Mech. Behav. Biomed. Mater.* **2014**, *37*, 109–124, doi:10.1016/j.jmbbm.2014.05.006.

118. Foley, P.L.; Henderson, A.L.; Bissonette, E.A.; Wimer, G.R.; Feldman, S.H. Evaluation of Fentanyl Transdermal Patches in Rabbits: Blood Concentrations and Physiologic Response. *Comp. Med.* **2001**, *51*, 239–244.

119. Colameco, S.; Coren, J.S. Opioid-Induced Endocrinopathy. *J. Am. Osteopath. Assoc.* **2009**, *109*, 20–25.

120. Katz, N.; Mazer, N.A. The Impact of Opioids on the Endocrine System. *Clin. J. Pain* **2009**, *25*, 170–175, doi:10.1097/AJP.0b013e3181850df6.

121. Ballantyne, J.C.; Mao, J. Opioid Therapy for Chronic Pain. *N. Engl. J. Med.* **2003**, *349*, 1943–1953, doi:10.1056/NEJMra025411.

122. Whitley, H.; Lindsey, W. Sex-Based Differences in Drug Activity. *Am. Fam. Physician* **2009**, *80*, 1254–1258.

123. Berkley, K.J. Sex Differences in Pain. *Behav. Brain Sci.* **1997**, *20*, 371–380, doi:10.1017/S0140525X97221485.

124. Craft, R.M. Sex Differences in Drug- and Non-Drug-Induced Analgesia. *Life Sci.* **2003**, *72*, 2675–2688, doi:10.1016/S0024-3205(03)00178-4.

125. Pleym, H.; Spigset, O.; Kharasch, E.D.; Dale, O. Gender Differences in Drug Effects: Implications for Anesthesiologists. *Acta Anaesthesiol. Scand.* **2003**, *47*, 241–259, doi:10.1034/j.1399-6576.2003.00036.x.

126. Ziemian, S.N.; Ayobami, O.O.; Kelly, N.H.; Holyoak, D.T.; Ross, F.P.; van der Meulen, M.C.H. Low Bone Mass Resulting from Impaired Estrogen Signaling in Bone Increases Severity of Load-Induced Osteoarthritis in Female Mice. *Bone* **2021**, *152*, 116071,

doi:10.1016/j.bone.2021.116071.

127. Ferretti, J.L.; Capozza, R.F.; Cointry, G.R.; García, S.L.; Plotkin, H.; Alvarez Filgueira, M.L.; Zanchetta, J.R. Gender-Related Differences in the Relationship between Densitometric Values of Whole-Body Bone Mineral Content and Lean Body Mass in Humans between 2 and 87 Years of Age. *Bone* **1998**, *22*, 683–690, doi:10.1016/S8756-3282(98)00046-5.

128. Kalervo Väänänen, H.; Härkönen, P.L. Estrogen and Bone Metabolism. *Maturitas* **1996**, *23*, S65–S69, doi:10.1016/0378-5122(96)01015-8.

129. Han, Z. □H.; Palnitkar, S.; Rao, D.S.; Nelson, D.; Parfitt, A.M. Effects of Ethnicity and Age or Menopause on the Remodeling and Turnover of Iliac Bone: Implications for Mechanisms of Bone Loss. *J. Bone Miner. Res.* **1997**, *12*, 498–508, doi:10.1359/jbmr.1997.12.4.498.

130. Turner, R.T.; Wakley, G.K.; Hannon, K.S. Differential Effects of Androgens on Cortical Bone Histomorphometry in Gonadectomized Male and Female Rats. *J. Orthop. Res.* **1990**, *8*, 612–617, doi:10.1002/jor.1100080418.

131. Feik, S.A.; Thomas, C.D.L.; Bruns, R.; Clement, J.G. Regional Variations in Cortical Modeling in the Femoral Mid-Shaft: Sex and Age Differences. *Am. J. Phys. Anthropol.* **2000**, *112*, 191–205, doi:10.1002/(SICI)1096-8644(2000)112:2<191::AID-AJPA6>3.0.CO;2-3.

132. Schlecht, S.H.; Pinto, D.C.; Agnew, A.M.; Stout, S.D. Brief Communication: The Effects of Disuse on the Mechanical Properties of Bone: What Unloading Tells Us about the Adaptive Nature of Skeletal Tissue. *Am. J. Phys. Anthropol.* **2012**, *149*, 599–605, doi:10.1002/ajpa.22150.

133. Burr, D.B.; Martin, R.B. The Effects of Composition, Structure and Age on the Torsional Properties of the Human Radius. *J. Biomech.* **1983**, *16*, 603–608, doi:10.1016/0021-9290(83)90110-0.

134. Martin, R.B.; Atkinson, P.J. Age and Sex-Related Changes in the Structure and Strength

of the Human Femoral Shaft. *J. Biomech.* **1977**, *10*, 223–231, doi:10.1016/0021-9290(77)90045-8.

135. Ruff, C.B.; Hayes, W.C. Sex Differences in Age-Related Remodeling of the Femur and Tibia. *J. Orthop. Res.* **1988**, *6*, 886–896, doi:10.1002/jor.1100060613.

136. Cannarella, R.; Barbagallo, F.; Condorelli, R.A.; Aversa, A.; La Vignera, S.; Calogero, A.E. Osteoporosis from an Endocrine Perspective: The Role of Hormonal Changes in the Elderly. *J. Clin. Med.* **2019**, *8*, 1564, doi:10.3390/jcm8101564.

137. Andronowski, J.M.; Depp, Randi M. *"A Multidisciplinary Perspective on the Role of Marginalization in the Identification of Opioid Users in Medicolegal Investigations." The Marginalized in Death: A Forensic Anthropology of Intersectional Identity in the Modern Era.*; 2022;

138. Weinstein, R.S.; Manolagas, S.C. Apoptosis and Osteoporosis. *Am. J. Med.* **2000**, *108*, 153–164, doi:10.1016/S0002-9343(99)00420-9.

139. Van Den Beld, A.W.; Kaufman, J.-M.; Zillikens, M.C.; Lamberts, S.W.J.; Egan, J.M.; Van Der Lely, A.J. The Physiology of Endocrine Systems with Ageing. *Lancet Diabetes Endocrinol.* **2018**, *6*, 647–658, doi:10.1016/S2213-8587(18)30026-3.

140. Ng, J.-S.; Chin, K.-Y. Potential Mechanisms Linking Psychological Stress to Bone Health. *Int. J. Med. Sci.* **2021**, *18*, 604–614, doi:10.7150/ijms.50680.

141. Yirmiya, R.; Goshen, I.; Bajayo, A.; Kreisel, T.; Feldman, S.; Tam, J.; Trembovler, V.; Csernus, V.; Shohami, E.; Bab, I. Depression Induces Bone Loss through Stimulation of the Sympathetic Nervous System. *Proc. Natl. Acad. Sci.* **2006**, *103*, 16876–16881, doi:10.1073/pnas.0604234103.

142. Riggs, C.M.; Vaughan, L.C.; Evans, G.P.; Lanyon, L.E.; Boyde, A. Mechanical

Implications of Collagen Fibre Orientation in Cortical Bone of the Equine Radius. *Anat. Embryol. (Berl.)* **1993**, *187*, doi:10.1007/BF00195761.

Appendices

Appendix A: The University of Akron IACUC (Animal protocol) approval form for the NIJ grant-funded rabbit-opioid experimental model project.

THE UNIVERSITY OF AKRON

MEMORANDUM

TO: Janna Andronowski

CC: IACUC@uakron.edu

FROM: Beth Kenaga, IACUC Administrator

DATE: November 23, 2019

SUBJECT: APPROVAL NOTICE FOR AR1
Protocol: 18-11-12 ARC
Titled: Longitudinal Effects of Prolonged Opioid Use on Cortical Bone Remodeling in a Rabbit Model

Your 1st Annual Review was approved by The University of Akron's Institutional Animal Care and Use Committee (IACUC) designated member review process on **November 21, 2019.**

A copy of this form will be filed with your protocol in the Research Office. If you have any questions, please contact Beth Kenaga, IACAUC Administrator, at 330-972-5845 or via email at bkenaga@uakron.edu.

Beth Kenaga
[redacted]
IACUC Administrator

The University of Akron operates under the Public Health Service (PHS) Assurance number A3870-01.

Appendix B: *GUI setup parameters (Beamtime - Sept. 2021)*

Imaging setup parameters via proprietary GUI (Beamtime - Sept. 2021)			
Camera Controls			
	Viewer low limit		20.0
	Exposure (msec)		100
	Dead time (msec)		10
	ROI first line		0
	ROI heigh, lines (max. 2160)		2160
	Viewer height limit		35000.0
	Frames per second		10.00
	Max fps. estimate		100
	ROI first column		0
	ROI width. Columns (max. 2560)		2560
	buffered		yes
	N buffers		3000
	Trigger		External
	Sensor pixel rate, Hz		286000000
	Add timestamp to camera frames		*Unchecked*
Various			
	Viewer low limit		20.0
	Viewer high limit		35000.0
Motor controls and indicators			
	CT Stage	CT stage	0.000
		-	180.000
		JOG-	20.000
	Sample Vertical	Vertical	0.000
		-/+ movement*	0.500
	Sample Horizontal	Horizontal	0.000

		-/+ movement*	0.000
Scan Controls			
	Outer loop	Vertical (mm)	
		Number of points	0
		Range	-0.0
		Or step size	0
		Endpoints	Check* include
			uncheck* after
	Inner loop	CT stage (deg)	
		Start position	0
		Number of points	3000
		range	180.0
		Or step size	0.06
Flat-field correction settings			
	Motor		horizontal
	Radio position (mm)		33.304
	Flat position (mm)		45
	Num of flats		100
	Num of darks		50
File-writer settings			
	Root dir:		*select directory*
	CT scans' name pattern		*sample ID*
	Use bigtiff containers		*unchecked*
	Separate scans		*checked*
	Filename pattern		Frame_{:>05}.tif

Appendix C: *GUI setup parameters (Beamtime - Sept. 2022)*

Imaging setup parameters via GUI (Beamtime - Sept. 2022)			
Camera Controls			
	Exposure (msec)		150
	Dead time (msec)		20
	ROI first line		0
	ROI heigh, lines (max. 2160)		2160
	Frames per second		5.00
	Max fps. estimate		100
	ROI first column		0
	ROI width. columns		2560
	buffered		yes
	N buffers		3000
	Trigger		EXTERNAL
	Add timestamp to camera frames		NONE
Various			
	Viewer low limit		100
	Viewer high limit		40000
Motor controls and indicators			
	Sample CT Stage	CT stage	0.000
		JOG-	5.000
	Sample Vertical	Vertical	0.000
		-/+ movement*	0.500
	Sample Horizontal	Horizontal	0.000
		-/+ movement*	0.000
Scan Controls			
	Outer loop	Vertical (mm)	
		Number of points	0

		Range	0
		Or step size	0
		Endpoints	Check* include
	Inner loop	CT stage (deg)	
		Flats	*checked* before
		Start position	0
		Number of points	3000
		range	180.0
		Or step size	0.06
		Motion	Checked* on the fly
Flat-field correction settings			
	Motor		horizontal
	Radio position (mm)		28.82
	Flat position (mm)		38.82
	Num of flats		100
	Num of darks		50
File-writer settings			
	Root dir:		*select directory*
	CT scans' name pattern		*sample ID*
	Use bigtiff containers		*checked*
	Number of images per bigtiff		3000
	Filename pattern		Frame_{:>05}.tif

Appendix D: *Raw SRμCT imaging data reconstruction using ufo-kit.*

Raw SRμCT imaging data reconstruction using ufo-kit

Centre of Rotation	
Auto: correlate first/last projections	*selected*
Auto: minimize STD of a slice	*not selected*
Search rotation axis in [start, stop, step] interval	1270.1290.1
Search in slide from row number	100
Size of reconstructed patch (pixel)	256
Define rotation axis manually	*not selected*
Axis is in column no [pixel]	1290
Increment axis every reconstruction	0.0
Use image midpoint (for half-acquisition)	*not selected*
Phase Retrieval	
Enable paganin/TIE phase retrieval	*not selected*
Photon energy [keV]	20
Pixel size [micron]	3.6
Sample-detector distance [m]	0.1
Delta/beta ratio: (try default if unsure)	200
Filters	
Threshold (prominence of the spot)	1000
Spot blur. Sigma [pixels]	2
Enable ring removal	*not selected*
Use ufo Fourier-transform based filter	*selected*
1D or 2D	2D
Sigma horizontal	3
Sigma vertical	1
Use sarepy sorting	*not selected*

Window size	21
Remove wide	*not selected*
window	91
SNR	3
Region of interest and histogram settings	
Select rows which will be reconstructed	*selected*
First row in projections	1000
Number of rows (ROI height)	20
Step (reconstruct every Nth row)	1
Clip histogram and save sleeves in	*not selected*
8-bit or 16-bit	8-bit
Min value in 32-bit histogram	0.0
Max value in 32-bit histogram	0.0
Crop slices	*not selected*
x	0 width, 0 y, 0 height
Rotate volume clockwise by [deg]	0.0
Input/output and misc settings	
Save argos in .params file	*selected*
Save slices in multiple tiffs	*not selected*
Load images and open viewer after reconstruction	*not selected*
Keep all temp data till the end of reconstruction	*not selected*
Preprocess with a generic ufo-launch pipeline, f.i.	*not selected*
Use common flats/darks across multiple experiments	*selected*

Appendix E: *Demonstrating complete list of parameters set for 3-point bend-tests using Instron E3000 and digital console using Wavematrix software program*

Instron E3000 3-point bend test parameter settings (March 2023)	
Setting	**Parameter set**
Test - Acquisition Setup	
Data acquisition rate	1000.0000 Hz
Resampling (anti-alias filter settings)	automatic
Filter type	butterworth
Filter corner frequency	200.0000 Hz
Filter order	4 pole
Test - Sequence	
Axial Waveform Step 1 - Absolute Ramp Waveform	
Control Mode	Position (Axial:Position)
Ramp mode	Rate
Ramp rate	1.0000 mm/s
End point (absolute value)	-30.0000mm
Waveform End Action	Finish cell, then wait for all
Waveform Channel Event Detector	Enabled
Channel to monitor	Load (AXIAL:Load)
Event Type	Feedback falls below threshold
Threshold Value	-5.0000N
Event Action	Finish Cell, then wait for all
AXIAL Wavelength Properties - Step 2 – Hold Waveform	
Control Mode	Position (AXIAL:Position)
Hold Duration	5.0000s
Waveform End Action:	Finish Cell, then wait for all
AXIAL Waveform Properties - Step 3 – Relative Ramp Waveform	
Control Mode	Position (AXIAL: Position)

Ramp Rate	1.0000 mm/min
End Point	-20.0000mm
Waveform End Action	Finish cell, then wait for all
Waveform channel event detector	Enabled
Channel to Monitor	Load (AXIAL:Load)
Event type	Feedback rises above threshold
Threshold Value	-2.0000N
Event Action	Finish cell, then wait for all
AXIAL Waveform Properties - Step 4 - Hold Waveform	
Control Mode	Position (AXIAL:Position)
Hold Duration	5.0000s
Waveform End Action	Finish Cell, then wait for all

Appendix F: SRμCT box plots to demonstrate distribution.

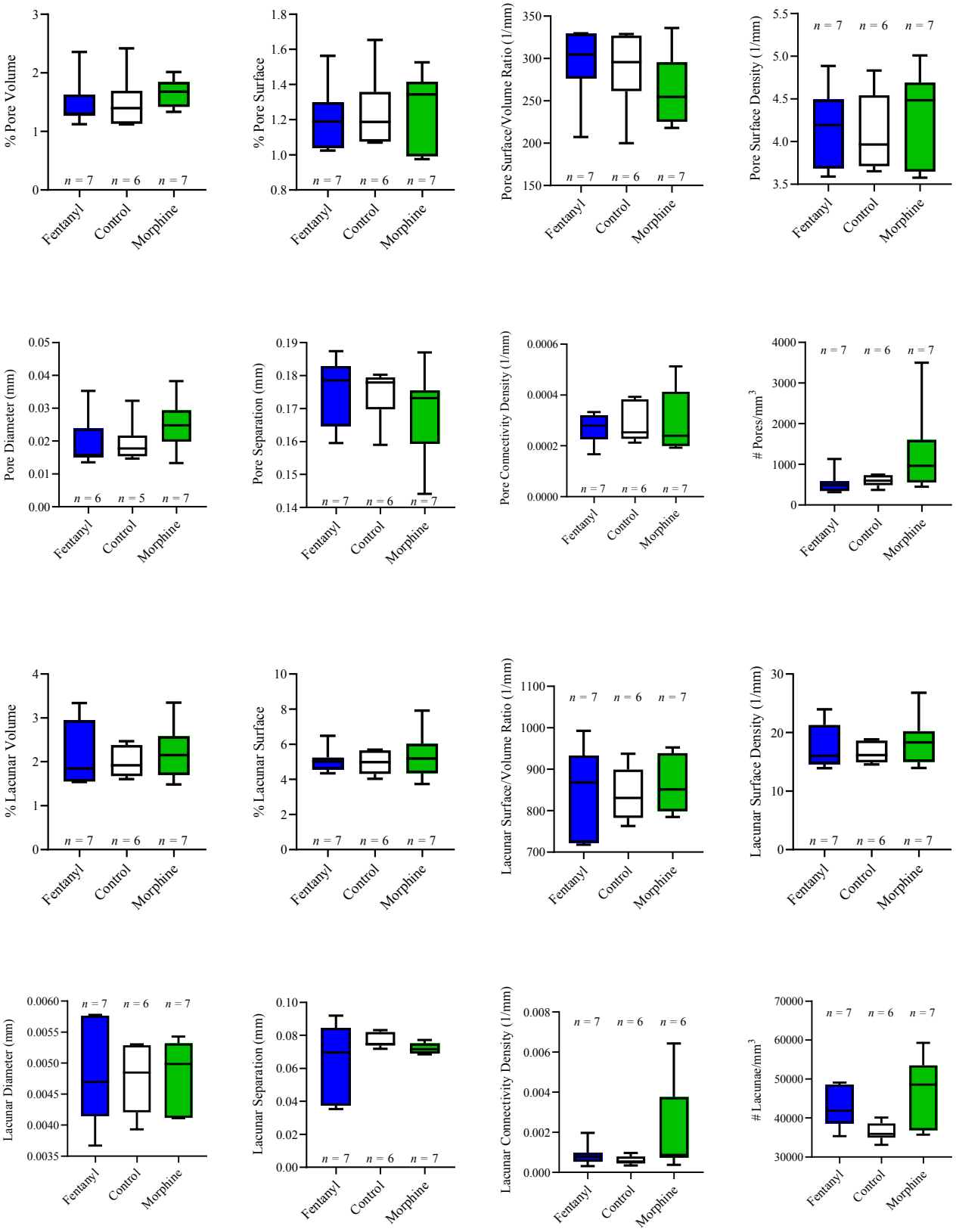

Appendix G: Cross-sectional geometry box plots to demonstrate distribution.

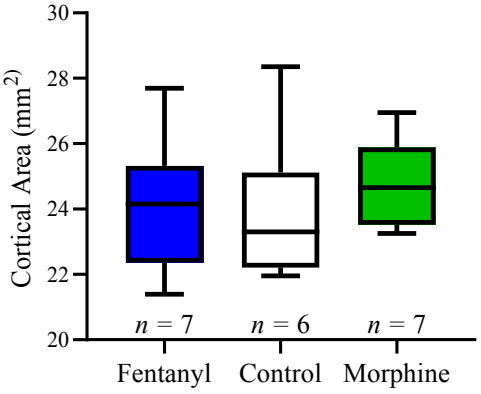

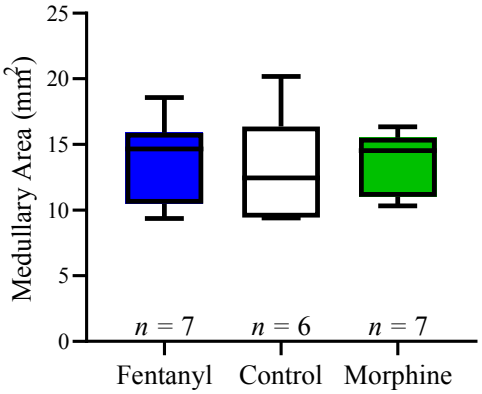

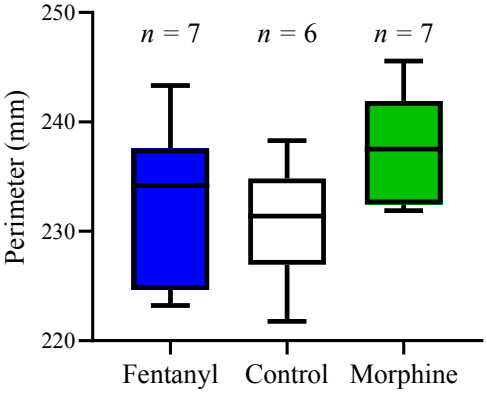

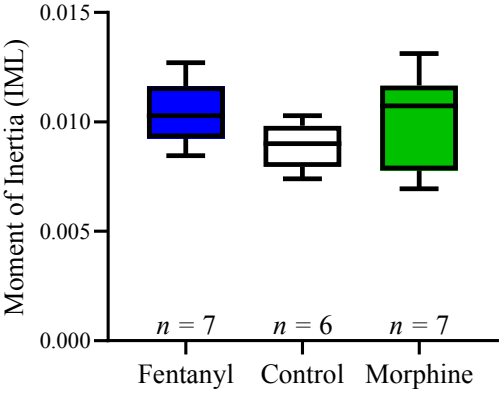

Appendix H: Biomechanical parameter box plots to demonstrate distribution.